scientific reports

Check for updates

OPEN

Impact of vaterite integration on the hydration, microstructure and performance of calcined clay cements

Mohammad H. Nofalah, Loucas Kyriakou, José M. Fernández, Íñigo Navarro-Blasco & José I. Álvarez✉

Vaterite Calcined Clay Cement (VC3) is a novel binder system in which the conventional calcite used in Limestone Calcined Clay Cement (LC3) is replaced with vaterite, a metastable polymorph of calcium carbonate characterized by its higher reactivity and spherical particle morphology. Although initial studies suggest potential benefits, the effects of vaterite on hydration kinetics, fresh-state behavior, and long-term mechanical performance remain insufficiently understood. To address this, eight mortar formulations were developed with 0–15% of vaterite content and 40%-50% Ordinary Portland Cement (OPC) content. Results showed that, in VC3 specimens, vaterite enhanced fresh-state workability and prolonged the induction period of hydration while maintaining long-term reactivity. Although early-age compressive strength was reduced, VC3 mortars exhibited significant strength development over time. At 91 days, the mortar incorporating 15% vaterite and 50% OPC showed a marked increase in strength, reaching 129% of the compressive strength of the LC3 reference mortar. Even formulations with only 40–45% OPC achieved 110–124% of the reference strength. Analysis of the phase assemblage and microstructural analyses confirmed sustained pozzolanic activity, with ongoing portlandite (CH) consumption and the formation of ettringite and carboaluminate phases. These results position VC3 as a promising low-clinker alternative, combining improved fresh-state performance with competitive long-term strength and enhanced sustainability.

Climate change remains one of the most pressing global challenges, driven largely by rising concentrations of anthropogenic greenhouse gases, particularly carbon dioxide (CO_2)[1]. As the second most consumed commodity after water, and as the backbone of development and urbanization[2,3], Ordinary Portland Cement (OPC) exceeds 4 gigatons in annual production, with demand projected to rise by 50% by 2050[4,5]. The construction industry, a major source of global carbon emissions, is under growing pressure to become more sustainable[6,7]. In response, substantial research efforts have focused on developing low-carbon cementitious binders to mitigate the environmental impact of the construction industry[8].

Supplementary cementitious materials (SCMs) such as ground granulated blast-furnace slag (GGBFS) and coal fly ash have played a vital role in decarbonization efforts. However, their limited availability restricts their global scalability[9–11] as GGBFS depends on declining steel production, while the shift away from coal-fired power plants reduces fly ash supply. In this context, Limestone Calcined Clay Cement (LC3) has emerged as a promising multi-component system that can replace up to 50% of OPC with abundant materials such as calcined clays and limestone[12,13]. The introduction of EN 197-5 by the European Committee for Standardization (CEN) in 2021 formally recognized LC3 under the classification CEM II/C-M(Q-LL), further legitimizing its application in industry[14].

LC3 is primarily composed of metakaolin (MK) and limestone, materials that are globally available and economically accessible. Its mechanical performance is comparable to, or even surpasses, that of OPC, due to its refined microstructure and the synergistic hydration between its components[15,16]. These effects are linked to the formation of calcium aluminosilicate hydrate (C-A-S-H) and additional AFm phases such as Hemicarboaluminate (Hc) and Monocarboaluminate (Mc), which enhance strength and durability[17]. Notably, LC3 formulations can reduce CO_2 emissions by up to 40% relative to OPC[18].

MATCH Research Group, Department of Chemistry, School of Sciences, University of Navarra, C/. Irunlarrea 1, Pamplona 31008, Spain. ✉email: jalvarez@unav.es

Traditionally, LC3 formulations use calcite as the source of calcium carbonate ($CaCO_3$). However, recent studies have proposed substituting calcite with vaterite, a metastable polymorph of $CaCO_3$ with higher surface reactivity and a spherical morphology, giving rise to Vaterite Calcined Clay Cement (VC3)[19]. According to the literature, vaterite's morphology improves the fresh-state workability, addressing one of LC3's key limitations compared to OPC[19], while its reactivity accelerates the formation of hydration products, leading to a denser microstructure and potentially greater long-term durability[19]. These changes are associated with increased formation of Hc, Mc, and Strätlingite, which further reinforce the cement matrix[19,20]. Among the polymorphs of $CaCO_3$, vaterite is thermodynamically less stable and exhibits a higher solubility product (Ksp = 1.58 . 10^{-8} at 25 °C) compared to the more stable calcite (Ksp = 3.98 . 10^{-9})[19]

$$AS_2 + (6.2 - 3.1a)CH + (12 - 4.6a)H \rightarrow (2 - a)\,C_{1.5}A_{0.1}SH_4 + aC_2ASH_8 + (0.8 - 0.9a)\,C_4AH_{13} \quad (1)$$

$$AS_2 + 5.8CH + 0.4\overline{CC} + 11.8H \rightarrow 0.8C_4A\overline{C0.5}H_{12} + 2C_{1.5}A_{0.1}SH_4 \quad (2)$$

$$AS_2 + 5.4CH + 0.8\overline{CC} + 12.2H \rightarrow 0.8C_4A\overline{CH}_{12} + 2C_{1.5}A_{0.1}SH_4 \quad (3)$$

*Phase notation: Metakaolin (AS_2), Portlandite (CH), Water (H), Calcium Carbonate ($C\overline{C}$).

From a sustainability standpoint, vaterite production has recently become more viable due to advancements in scalable and cost-effective synthesis techniques[21]. These include methods that capture atmospheric CO_2 or carbon from industrial sources, reducing embodied carbon to as low as 0.3 kg CO_2 per kg of vaterite produced. Moreover, up to 0.44 kg of CO_2 can be sequestered during vaterite formation, presenting the possibility of a negative carbon footprint[19]. Also, Zeppa[22] reported that that even when accounting for the CO_2 emissions associated with generating heat and electricity for production, as well as the transport of the product to the customer, the mineralization of flue gases into precipitation has been shown to deliver a net reduction of 229 kg CO_2 per tonne of produced material. This result aligns closely with the overall carbon footprint reported by Mattila et al. for industrial-scale calcium carbonate precipitation[23].Additional research has demonstrated that vaterite can be synthesized from industrial residues such as recycled concrete fines[24], steel slag[25], carbide slag[26], and magnesium slag[27], often through leaching-carbonation processes[28].

LC3 binding systems have been thoroughly studied in terms of mechanical strength[18–21,29], durability[30,31], mix design optimization[32–34], fresh-state behavior[35–37], hydration kinetics[33], interactions between calcined clay and limestone[12], phase assemblages[38,39], metakaolin reactivity[40,41], and pore structure evolution[42]. Although several studies have examined the effect of vaterite as a SCM on hydration, microstructure, and performance[20,22,41–43], the investigated matrices have primarily involved sulfoaluminate cements, blends containing waste or recycled aggregates, or systems designed for the incorporation of waste materials. Although VC3 exhibits promising characteristics, its performance has not yet been systematically assessed. To the best of our knowledge, only one study has thus far investigated the incorporation of vaterite into LC3, focusing on three ternary mixtures comprising vaterite, OPC, and clay, and evaluating their behavior only up to 28 days of curing[19] while the long-term performance of VC3 systems remained poorly understood.

This study addresses this gap by providing a detailed evaluation and explain the fundamental hydration mechanisms of VC3 mortars, particularly focusing on the role of mineral physico-chemical characteristics on properties development of the material. While previous research emphasized mid-term behavior and limited number of mixtures[19], the current study investigates a broader scope of binder compositions and employs a vaterite with a lower specific surface area to evaluate its long-term influence. This approach reveals a divergence from short-term trends, specifically demonstrating that such characteristics prove advantageous to the binder's development at medium and long curing ages. To address phenomena that remain under-explored in existing studies, the relationship between the surface zeta potential of calcite and vaterite, their respective affinities for calcium and sulfate ions, and their influence on early-age nucleation and hydration of this VC3 matrices, has been examined. By systematically evaluating the interplay between particle morphology, hydration kinetics, and microstructural assemblages, this research seeks to establish a scientific basis for better understating the fresh and hardened properties and also the sustainability and durability of VC3 as a next-generation binder.

Materials and methods

Materials

The materials used in this study included a commercially available CEM I 52.5 R cement (CE and NF certified), supplied by Grupo Cementos Portland Valderrivas. Metakaolin (Metaver N) was sourced from NEWCHEM. Calcium carbonate (calcite, CACB-00 A) and gypsum (CASU-02 A), both with >99% purity, were obtained from Labkem. Standardized CEN sand (Table S1), complying with EN 196-1 specifications[43], was used for mortar preparation.

Vaterite was synthesized in the laboratory using a controlled precipitation method, achieving a purity of 98 ± 2%; details of the synthesis procedure are provided in Sect. "Vaterite synthesis". Table 1 summarizes the chemical composition and physical characteristics, and Fig. 1 illustrates particle size distribution (PSD) parameters of the raw materials. Scanning electron microscopy (SEM) images of the synthesized vaterite are shown in Fig. 2, while Fig. 3 presents its morphology and particle size as observed through transmission electron microscopy (TEM). The crystalline phases of calcium carbonates, determined via X-ray diffraction (XRD), are presented in Fig. 4.

A polycarboxylate ether-based (PCE) superplasticizer (MasterCast GT 205), supplied in powder form, was used in all mixtures. It has a density of 0.870–0.970 g/cm³ and an average molecular weight of 8000 g/mol.

Raw material	CaO (%)	SiO_2 (%)	Al_2O_3 (%)	Fe_2O_3 (%)	K_2O (%)	Na_2O (%)	MgO (%)	SO_3 (%)	LOI* (%)	Dv, 10 (µm)	Dv, 50 (µm)	Dv, 90 (µm)
Cement	68.8	16.0	5.0	2.1	1.1	0.2	1.8	3.8	2.8	0.3	11.3	26.4
MK	0.3	45.9	48.6	0.9	0.9	1.0	1.7	n.d.	0.9	0.3	2.5	11.3
Gypsum	40.6	2.0	1.2	n.d.	0.1	n.d.	1.6	52.4	21.2	10.5	41.7	89.4
Calcite	55.2	0.3	n.d.	n.d.	0.1	n.d.	0.1	n.d.	44.8	0.2	2.9	4.9
Vaterite	54.3	0.3	n.d.	n.d.	0.8	n.d.	0.1	n.d	46.0	0.3	9.1	17.9

Table 1. Chemical composition and physical characteristics of the raw materials (wt%). *LOI: Loss of ignition, determined by TGA; n.d.: not detected, below the detection limit.

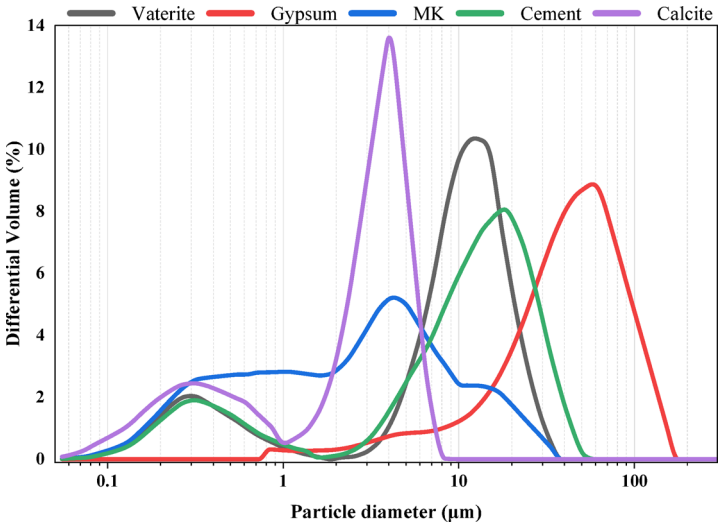

Fig. 1. Particle size distribution curves of the raw materials, measured by laser diffraction.

Methods

Vaterite synthesis

Vaterite was synthesized in the laboratory using a controlled aqueous precipitation method at room temperature (25 °C). Two separate solutions were prepared: a 4 M solution of potassium carbonate (K_2CO_3) in distilled water, and a mixed 2 M solution of calcium chloride ($CaCl_2$) and ammonium chloride (NH_4Cl), also in distilled water. The K_2CO_3 solution was rapidly added to the $CaCl_2$–NH_4Cl solution in a 2:1:1 molar ratio (K_2CO_3:$CaCl_2$:NH_4Cl) under continuous stirring at 600 rpm. The mixture was stirred for 10 min to promote the complete precipitation of calcium carbonate. Then, the resulting suspension was immediately filtered using a Buchner funnel and a paper filter to isolate the solid product. The filtered precipitate was rinsed with a small amount of distilled water, followed by rinsing with 70% ethanol to inhibit further crystallization and limit transformation. Then the resulting product was dried in an oven at 80 °C for 24 h.

Physicochemical and surface characterization of raw materials

The chemical composition of the raw materials listed in Table 1 was determined using with a Bruker S2 Puma spectrometer (Bruker Scientific Instruments, Billerica, MA, USA). Measurements were performed under a helium atmosphere using a 4 µm polypropylene filter and an X-ray tube with a silver anode. Quantitative analysis was performed using Spectra Results Manager software (Bruker AXS Spectra Elements v2.3).

The particle size distribution of the raw materials was measured by laser diffraction using a Malvern Mastersizer (Malvern Panalytical Ltd., Malvern, UK).

The specific surface area of the samples was determined by nitrogen adsorption using the Brunauer-Emmett-Teller (BET) method on a Micromeritics ASAP 2020 Surface Area and Porosity Analyzer (Micromeritics Instrument Corp., Norcross, GA, USA). Approximately 0.2–0.3 g of each sample was degassed under vacuum, first at 90 °C for 1 h and then at 200 °C for 4 h, with a heating rate of 10 °C/min. Nitrogen adsorption measurements were conducted at − 196 °C over a relative pressure (P/P_0) range of 0.05 to 0.30. BET surface area values were calculated using the instrument's dedicated software (ASAP 2020 V4.00).

Zeta potential measurements were conducted using a ZetaProbe analyzer (Colloidal Dynamics, New Castle, DE, USA) equipped with a flow-through sensor (S/N: 684), operating at a minimum frequency of 0.30 MHz. Data acquisition and analysis were performed using ZetaProbe software version 2.14c Polar. Suspensions of calcium carbonate were prepared by dispersing 10 wt% of vaterite and calcite powders in 140 mL of distilled water under continuous stirring. The prepared suspensions were then introduced into the flow-through cell of the device. During the test, pH and electrical conductivity were continuously monitored. Potassium sulfate

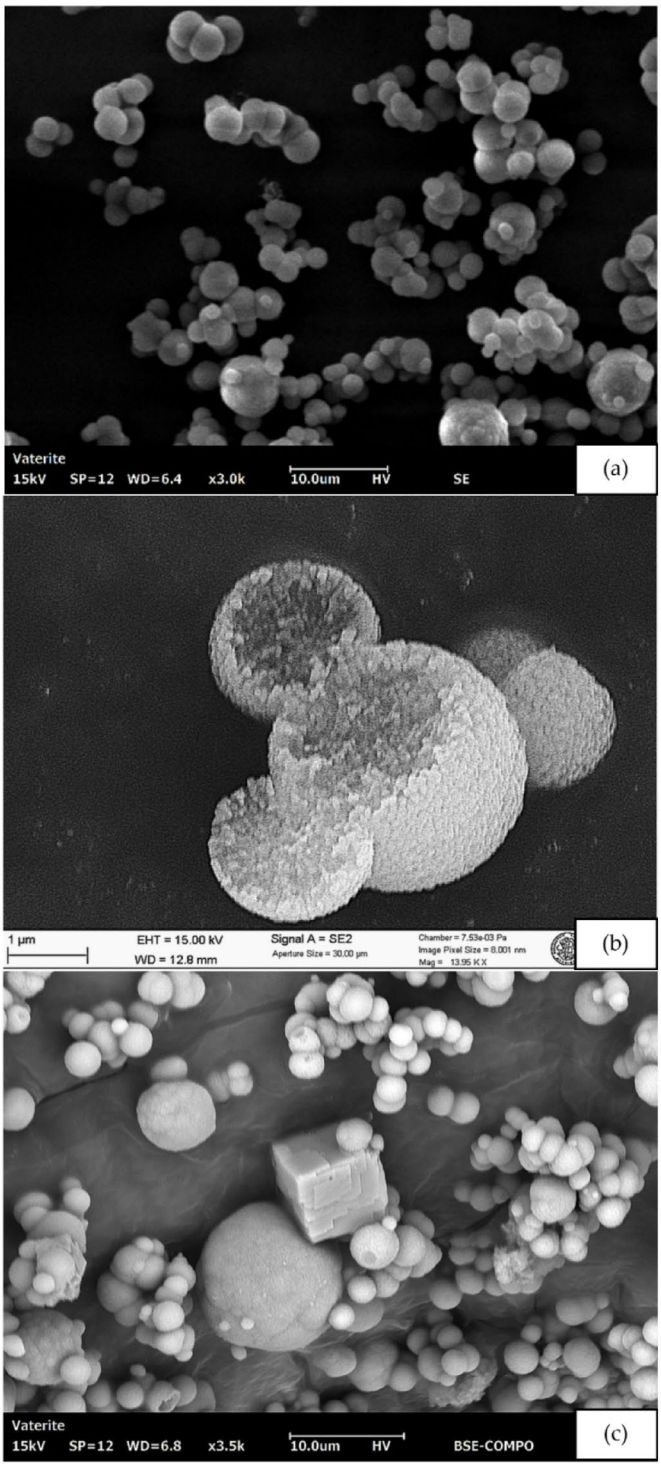

Fig. 2. SEM images of synthesized vaterite showing particle morphology and size at different magnifications: (**a**) SE at 3000x, (**b**) SE at 13, 950x, (**c**) and BSE at 3500x.

(K_2SO_4) and calcium chloride ($CaCl_2$) solutions, each with a concentration of 1 mol/L, were used as titrants and gradually added to the suspension in a controlled manner.

The cement pore solution, prepared to simulate the pore fluid chemistry of OPC, CEM I at a water-to-cement ratio of approximately 0.5, followed the composition reported by Baueregger et al.[44]. It was made by dissolving 1.72 g of $CaSO_4{\cdot}2\ H_2O$, 6.96 g of Na_2SO_4, 4.75 g of K_2SO_4, and 7.12 g of KOH in deionized water, resulting in approximate ion concentrations (g/L) of K^+: 7.1, Na^+: 2.2, Ca^{2+}: 0.4, SO_4^{2-}: 8.2, and OH^-: 1.0. The same procedure applied by the $CaCl_2$ and K_2SO_4 solutions was also followed for the cement pore solution and Zeta potential measurements were recorded throughout the titration process.

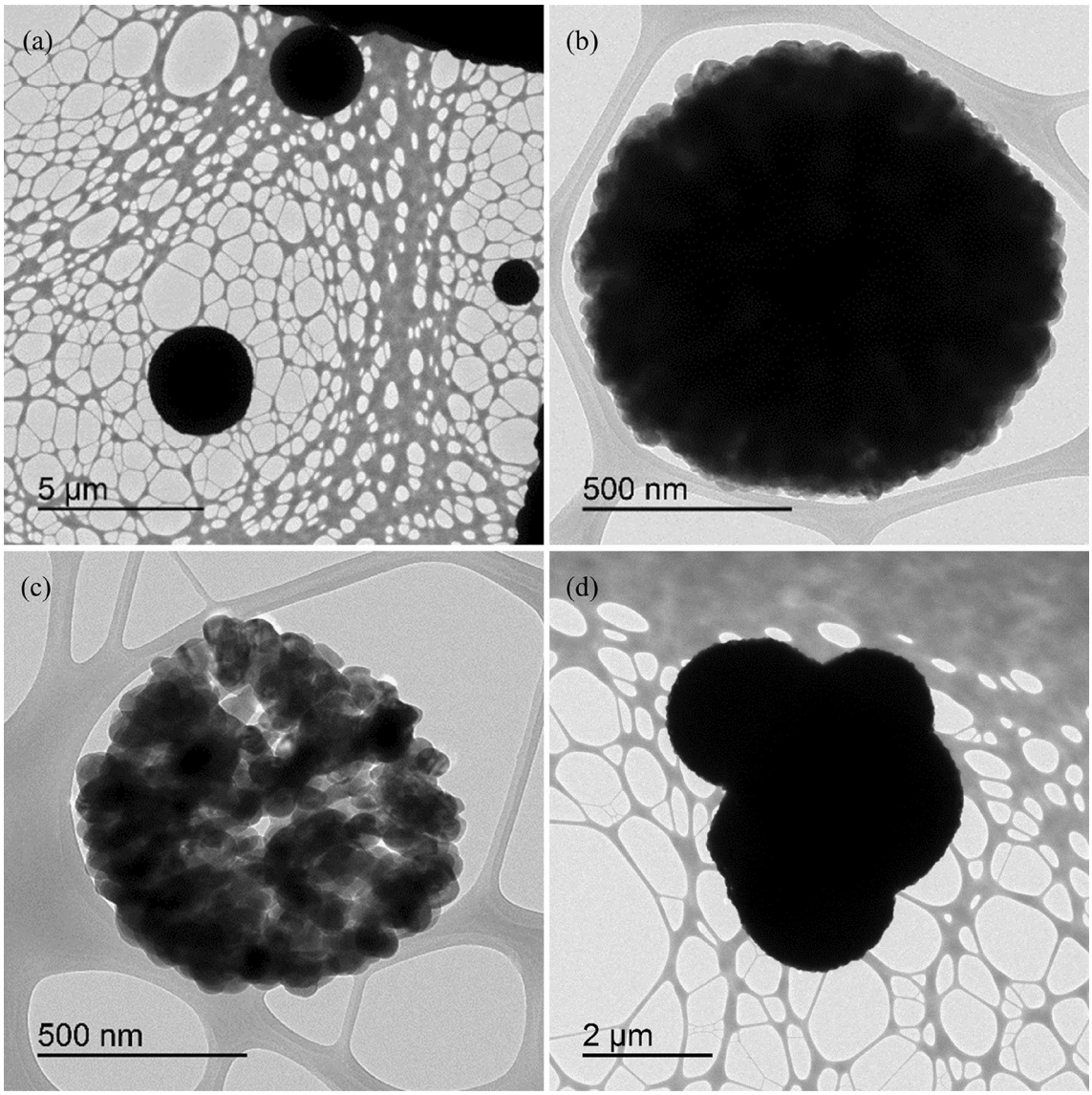

Fig. 3. TEM images of synthesized vaterite particles showing morphology and particle size: (**a**, **b**) spherical morphology, (**c**) porous structure from individual particles agglomeration, and (**d**) particle agglomeration of the spheres.

Mortar preparation

Eight mortar compositions were prepared for this study: Seven VC3 and blended formulations, and one Limestone calcined clay cement mortar used as a control. All mixtures were designed with a fixed water-to-binder ratio (W/B) of 0.5 and a sand-to-binder ratio of 3:1 by weight.

The primary aim was to evaluate the influence of replacing calcite with vaterite in LC3-based mixtures. For this purpose, V0 (LC3), VC3-5, VC3-10, and VC3-15 mixtures were studied as the first set of samples. A reference mortar, LC3 (designated V0), served as a baseline for comparison. In C45V20, C45V15, C40V25, and C40V15 mixtures as the second set, the cement content was reduced to 40% and 45%, with corresponding adjustments in the proportions of metakaolin and vaterite. This standardized mix design approach allowed for direct comparison of the impact of each component on fresh and hardened properties. Table 2 presents the detailed mix proportions and material compositions for all formulations.

For fresh mortar preparation, the dry components (standard sand, metakaolin, gypsum, calcite, vaterite, and superplasticizer) were blended in a solid additives' mixer (Model BL-8-CA, Lleal, S.A., Granollers, Spain) for 5 min to ensure homogeneity. Water was then gradually added and mixed at low speed for a duration exceeding 270 s using a Proeti ETI 26.0072 mixer (Proeti, Madrid, Spain). The fresh mortars were cast into cylindrical PVC molds (Ø = 30 mm, h = 40 mm) according to previous works[38] and cured in a climatic chamber at 95 ± 5% relative humidity and 20 ± 2 °C for up to 91 days. For the compressive strength tests, three specimens were measured at each curing age to ensure reproducibility and statistical significance. Additionally, one specimen per curing age was freeze-dried to arrest the progression of carbonation and hydration reactions and used for X-ray

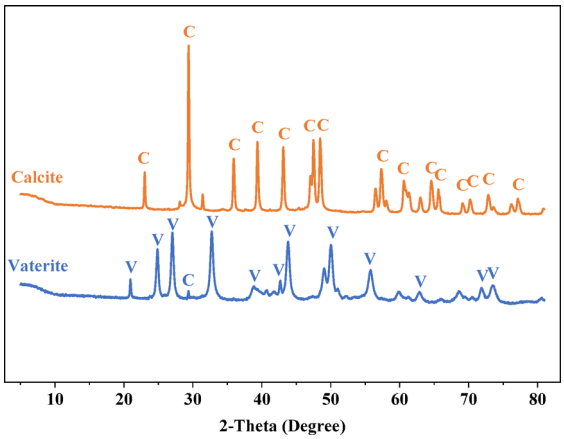

Fig. 4. XRD patterns of $CaCO_3$ polymorphs: calcite and synthesized vaterite. C corresponds to the calcite ICDD pattern (753446)[60], and V to vaterite pattern (15879)[61].

Name	Binder					PCE (%)	Water/binder	Sand/binder
	Cement (%)	MK (%)	Vaterite (%)	Calcite (%)	Gypsum (%)			
V0 (LC3)	50	30	0	15	5	0.2	0.5	3
VC3-5	50	30	5	10	5	0.2	0.5	3
VC3-10	50	30	10	5	5	0.2	0.5	3
VC3-15	50	30	15	0	5	0.2	0.5	3
C45V20	45	30	20	0	5	0.2	0.5	3
C45V15	45	35	15	0	5	0.2	0.5	3
C40V25	40	30	25	0	5	0.2	0.5	3
C40V15	40	40	15	0	5	0.2	0.5	3

Table 2. Mix proportions of mortar formulations (by weight% of binder components).

diffraction, thermogravimetric analysis, and microstructural investigations. The freeze-drying process involved immersion in liquid N_2 for 5 min, followed by sublimation at − 40 °C under 1 Pa vacuum for 24 h, ensuring the preservation of the mortar's microstructure[45].

Fresh state tests

Workability was assessed using the flow-table test in accordance with UNE-EN 1015-3[46]. Fresh mortar was placed in a truncated cone mold (100 mm base diameter, 70 mm top diameter, and 60 mm height) in two layers, each compacted with a tamping rod. The mold was lifted, and the flow table was dropped 15 times at a constant frequency to spread the mortar, after which the diameter was measured to determine workability. Setting times of mortar mixtures, measured according to the UNE-EN 1015-9 standard[47] by testing mortar resistance to penetration at regular intervals after mixing until a 0.5 N/mm^2 is reached. This determines the time during which the mortar remains workable before initial setting begins.

Isothermal calorimetry test

Hydration kinetics were monitored using an 8-channel TAM Air isothermal calorimeter at 25 °C over a 3-day period. 20 g of pastes were prepared by mixing distilled water with the binders (see Table 2) using a vertical-axis high-shear blender at 1600 rpm for 2 min. The fresh pastes were sealed in glass ampoules and then inserted into the calorimeter.

Compressive strength development

Compressive strength was measured after 91 days of curing using a Frank/Controls 81,565 press equipped with a Proeti ETI 26.0052 compressive breaking device. The tests were conducted at a breaking speed ranging from 20 to 50 N/s, with a 30–90 s time interval on cylindrical specimens, following the ASTM C39 standard[48].

Sustainability indicator

The development of eco-friendly construction materials should focus on minimizing environmental impact, besides considering material performance as a crucial parameter. Sustainability is more effectively represented when both environmental impact and performance are evaluated in conjunction. In this study, the replacement of calcite and the reduction of OPC content were assessed to quantify and compare the environmental efficiency and mechanical performance of different mixtures. This evaluation is expressed as a Sustainability Indicator (S_i),

defined as the ratio of CO_2 emissions associated with the binders to the compressive strength of the mortar at 91 days (Eq. 4). A lower ratio indicates a more sustainable mixture. The CO_2 emissions for each constituent were calculated based on previously reported data and life cycle assessment (LCA) studies (Table 3).

While the primary objective of this study was to characterize the fundamental material properties and hydration mechanisms of the resulting blended matrices, the laboratory synthesis route was optimized for phase purity rather than CO_2 footprint. For this reason, high-purity laboratory-grade reagents were utilized to ensure experimental repeatability and to minimize the influence of uncontrolled mineralogical impurities on the hydration results. The CO_2 emission factors selected for the Sustainability indicator calculation reflect industrial-scale production and carbon capture and utilization (CCU) pathways. Specifically, the negative emission factor for vaterite is based on established literature[19,21–23], representing its potential as a carbon-sequestering agent in a commercial context. Since vaterite as a supplementary cementitious material is an emerging field and high-resolution LCA data can vary based on synthesis pathways, this study adopts a conservative estimation approach by utilizing we utilized the lowest carbon sequestration values reported in current literature as the reference for our calculations. This ensures that the environmental benefits reported for the VC3 systems are not over-estimated and remain valid even under conservative industrial scenarios. In any case, this indicator should be regarded as a simplified comparative estimation.

$$S_i\left(\frac{kgCO_2}{MPa}\right) = \frac{CO_2 emissions/100\ kg\ Solids}{91 - days\ compressive\ strength} \tag{4}$$

Phase assemblage

Phase identification was performed on powdered samples using a Bruker D8 Advance diffractometer (Bruker Scientific Instruments, Billerica, MA, USA) with Cu $K\alpha_1$ radiation. Scans were conducted from 5° to 80° (2θ) with a step size of 0.03° and a dwell time of 1 s per step. The studies were carried out in pastes prepared with the same proportions indicated in Table 2, but without sand to avoid the intense diffraction peaks of the quartz. All samples were finely ground to an optimal particle size (< 5μm) to minimize preferred orientation effects, which is crucial for accurate quantification. Qualitative phase identification was conducted using Diffrac.EVA software (version 4.3.0.1, Bruker AXS). For quantitative phase analysis (QPA), 10 wt% of corundum (Al_2O_3) was intimately blended into the powdered pastes and used as an internal standard. Phase quantification was then performed using the Rietveld method implemented in the TOPAS V6 software (Bruker AXS), utilizing the corundum standard to determine the absolute weight fractions of all identified crystalline phases. The refinement strategy included the use of a fundamental parameters approach for peak shapes. The preferred orientation (PO) for portlandite and AFm phases was addressed through a systematic manual evaluation of the hkl directions. The quality of the fit was high across the entire experimental series, with a representative weighted profile R-factor (R_{wp}) between 3.21% and 3.64% and a goodness-of-fit (GOF) in the range of 2.48–2.86. Absolute phase abundances were determined using 10 wt% corundum as an internal standard, with estimated standard deviations (ESD) typically ranging from ± 0.3 wt% for low-abundance phases to ± 0.8 wt% for major hydration products.

Thermogravimetric analysis was performed using a TA Instruments SDT650 system (New Castle, DE, USA), with data processing via TRIOS software. Approximately 10 mg of each sample was placed in 90 μL alumina pans. Samples were heated from 35 °C to 1100 °C at a rate of 20 °C per minute under a nitrogen atmosphere with a flow rate of 100 mL per minute. The interpretation of the curves is guided by established literature[54,55].

Microstructural studies: scanning/transmission electron microscopy (SEM/TEM)

Microstructural characterization was carried out using two SEMs: COXEM EM-30 N (COXEM Co., Ltd., Daejeon, Republic of Korea) and ZEISS Sigma 300 VP FE-SEM. Fractured surfaces of hardened mortars were mounted on silver-pasted or carbon-taped stubs and gold-coated using a COXEM SPT-20 Ion Coater (COXEM Co., Ltd., Daejeon, Republic of Korea) at 4 mA for 120 s. Elemental analysis was conducted with a Quantax Compact 30 Bruker energy-dispersive X-ray spectrometer (Bruker Nano GmbH, Berlin, Germany), and data were processed using Esprit Compact software (version 2.3.1.1019, Bruker). Transmission electron microscopy TEM was performed using a JEOL JEM-1400 Plus microscope operating at 120 kV, equipped with an ORIUS GATAN SC600 camera for image acquisition, and images were acquired and processed using DigitalMicrograph 1.80.70 within the Gatan Microscopy Suite (GMS) version 1.8.0.

Results and discussion

Characterization of the synthesized vaterite

Figure 1 presents the particle PSD of the synthesized vaterite and calcite. The BET surface areas, determined from N_2 adsorption measurements, were 14.55 m^2/g for calcite and 7.52 m^2/g for vaterite. SEM and TEM images (Figs. 2 and 3) demonstrate that vaterite particles predominantly exhibit a spherical and porous morphology. The average size of the individual primary vaterite particles is approximately 75 nm, as observed by TEM; however, they display a pronounced tendency to agglomerate (Figs. 2b and 3b–c), forming secondary spherical structures.

Material type	Cement	Calcined clay	Calcite	Vaterite	Gypsum
Conversion factors for calculating CO_2 emissions ($kgCO_2eq./kg$)	0.86 [49–51]	0.11 [49,52]	0.005 [49,53]	− 0.14 [49–51]	0 [49]

Table 3. CO_2 emission for the materials used in this study.

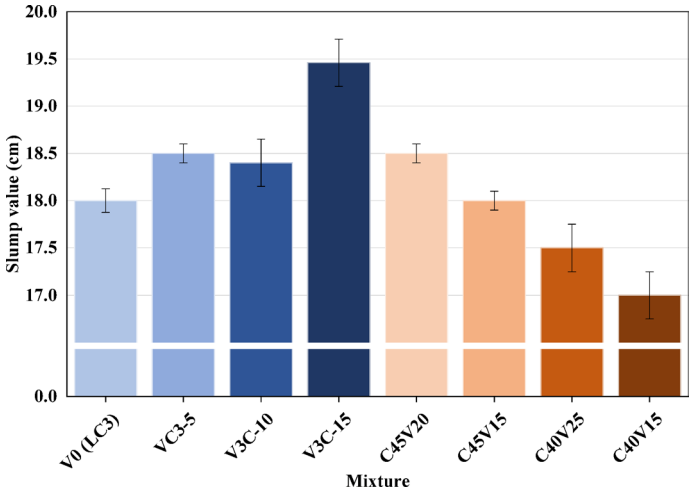

Fig. 5. Flow-table results of mortar mixtures, measured according to the UNE-EN 1015-3 standard.

Mixture	V0	VC3-5	VC3-10	VC3-15	C45V20	C45V15	C40V25	C40V15
Setting time (min)	91	94	105	119	114	104	84	76

Table 4. Setting times of mortar mixtures, measured according to the UNE-EN 1015-9 standard.

These agglomerated vaterite spheres, in turn, show further adhesion to one another, as evidenced in Figs. 2a and 3b. The size distribution values obtained by laser diffraction (Fig. 1) predominantly reflect the secondary agglomeration of the spherical particles. In line with these findings, previous literature has shown the formation of the primary and secondary vaterite particles and highlighted the propensity of vaterite spheres to undergo agglomeration[56]. The characterization of the vaterite particles in this work yielded findings entirely consistent with values reported in earlier investigations, including the particle size of the primary and secondary vaterite spheres obtained in this study, the D_{50} value of the particle size distribution, the roughness of the spheres, and the specific surface area[56–59].

The X-ray diffraction patterns of (Fig. 4) confirm the successful synthesis and high phase purity of the vaterite, being the predominant phase with a very tiny amount of calcite. The loss on ignition (LOI), determined via thermogravimetric analysis, was 44.79% for calcite and 46.03% for vaterite. These values correspond closely to the theoretical CO_2 content of pure calcium carbonate, with complete decomposition generally occurring around 800 °C. The observed LOI values also confirm the purity of both calcium carbonate powders (Table 1).

Flow-table test

Figure 5 presents the results of the flow-table test, illustrating the fluidity of the different binder systems. Both LC3 and VC3 mortars exhibit lower fluidity than the OPC mixtures[19], confirming that a reduction in OPC content generally decreases mortar fluidity. Among the alternative binders, replacing cement with metakaolin led to a more pronounced reduction in the slump values of the flow table compared to vaterite, as shown in the results presented in Fig. 5. Since metakaolin increases water demand and promotes flocculation by enhancing inter-particle interactions[62]. Specifically, at 45% cement content, increasing metakaolin from 30% to 35% decreased the slump from 18.5 cm to 18.0 cm. Similarly, at 40% cement, raising metakaolin content from 30% to 40%, reduced the slump from 17.5 cm to 17.0 cm.

VC3 mortars demonstrated higher flowability than LC3 mixtures, particularly those with higher vaterite content, as shown by flowability values of 18.5, 18.4, and 19.5 cm for VC3-5, VC3-10, and VC3-15, respectively, compared to 18.0 cm for the V0 (LC3) mixture (Fig. 5). This trend indicates that increasing vaterite content in the binder tends to improve flowability relative to the calcite-containing LC3 system. This improvement is attributed to the spherical morphology of vaterite, observed in Figs. 2 and 3, which contrasts with the finer and more angular particles of calcite[19,63].

Setting time and isothermal calorimetry studies

According to the literature, OPC mortars exhibit longer setting time compared to binders containing calcined clays[19,64]. As shown in Table 4, LC3 sets faster than VC3 when prepared with identical proportions, exhibiting setting times of 91 min and 119 min, respectively. In general, mortars with lower cement content exhibited shorter setting times. However, VC3 mixtures consistently set later than their LC3 counterparts. This behavior is attributed to the distinct surface-kinetic interactions of the two polymorphs rather than a lower chemical reactivity of vaterite.

An increase in vaterite content was also associated with longer setting times, showing setting times of 94, 105, and 119 min for VC3-5, VC3-10, and VC3-15, respectively. This behavior may be attributed to vaterite's particle size and its higher ion adsorption capacity, factors likely contributing to lower initial dissolution rate and delayed chemical participation in the formation of carboaluminate phases, which subsequently delay the precipitation of hydration products relative to calcite. These findings, discussed in Sect. "Flow-table test", illuminate the complex interplay between cement content, calcium carbonate polymorph, and particle characteristics in influencing the setting behavior of blended binders.

The isothermal calorimetry analysis of the V0 (LC3), VC3-5, VC3-10, and VC3-15 mixtures revealed significant differences in hydration behavior.

The LC3 mixture exhibited a shorter induction period compared to the VC3 systems, confirming that the presence of calcite particles tends to shorten the induction phase of hydration[63]. Among the vaterite blended binders, the duration of the induction period followed the trend: VC3-15 > VC3-10 > VC3-5, indicating faster initial hydration in mixtures with higher calcite content. This trend is primarily driven by the superior heterogeneous nucleation potential of the calcite surface for C-S-H and ettringite. While the smaller particle size of the calcite provides a higher specific surface area for these reactions[16], the surface-chemical characteristics of the $CaCO_3$ polymorph are the dominant factor. Specifically, the vaterite surface sequesters ions through adsorption (as supported by our Zeta Potential results), which retards the attainment of the critical supersaturation levels required to terminate the induction period.

The main hydration peak, which is primarily associated with the hydration of C_3S[65]. A delay was observed with increasing vaterite content, which shows slow dissolution and delays subsequent hydration reactions. As shown in Fig. 6, the sulfate depletion point, occurring shortly after the silicate peak, was most distinct in the V0 (LC3) mixture and became progressively less pronounced with increasing vaterite content. V0 (LC3) reached this transition point earlier than the other blended binder systems.

A similar trend was observed in the intensity of the aluminate peak (Second peak), which decreased in the order: V0 (LC3) > VC3-5 > VC3-10 > VC3-15. While differences between V0 (LC3), VC3-5, and VC3-10 were relatively small, a more marked reduction in peak intensity and delay in timing was noted between VC3-10 and VC3-15 (with no calcite and 5% more vaterite). Detailed characteristics of the aluminate peaks are summarized in Table.S2 and illustrated in Fig. S1 (Supplementary material). These findings align with previous studies reporting delayed aluminate reactions in the presence of coarser or less reactive carbonate phases[63]. Cumulative heat results further demonstrated that among the binders, those with higher calcite content released more heat during the first three days of hydration, indicating greater early-age reactivity.

The results shown in Fig. 6 indicate that within the VC3 series, increasing the vaterite content led to a progressive delay in both the main and aluminate peaks. These trends underscore the significant influence of vaterite on the hydration kinetics of the blended systems, impacting both the timing and intensity of the

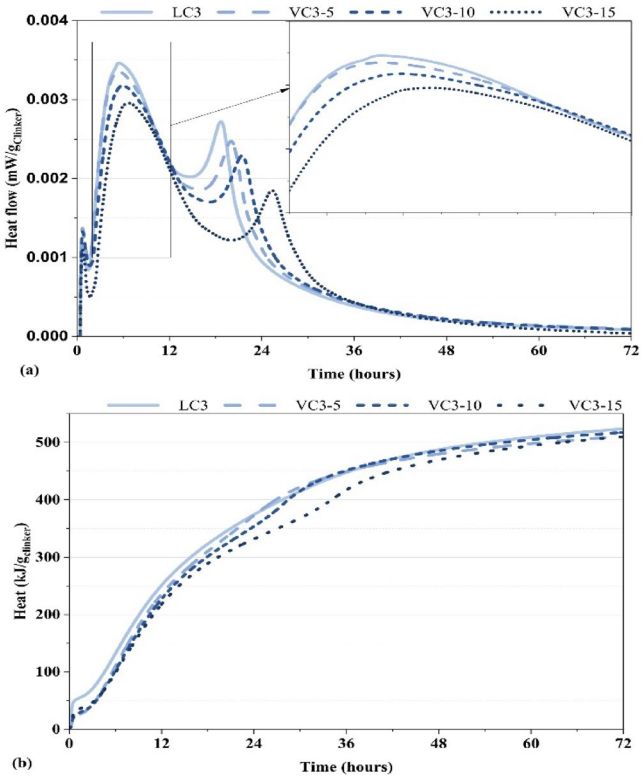

Fig. 6. Isothermal calorimetry results of the paste mixtures, normalized by clinker content: (**a**) heat flow during hydration, (**b**) cumulative heat release.

hydration reactions. The cumulative heat curves further reveal that, over the first three days, the heat release (normalized by clinker content) differs notably between LC3 and the VC3 blended binders, primarily due to variations in the aluminate reaction.

As vaterite content increases in calcined clay cement mixtures, the aluminate peak observed in isothermal calorimetry displays a progressively longer reaction duration, as shown in Table S2. The peak consistently shifts to later times, indicating a delayed onset of aluminate-related hydration processes. Although the peak integral decreases slightly with increasing vaterite content, it remains within a comparable range across all formulations. In contrast, the amplitude of the aluminate peak steadily declines, suggesting a reduction in the intensity of the reaction. These trends indicate that the total hydration energy is not significantly reduced but is instead distributed over a longer period. Since the peak width closely follows the same trend as the reaction duration (range), it was considered redundant and excluded from separate analysis.

A comparison of aluminate peak characteristics among C45V20, C45V15, C40V25, and C40V15 mixtures, alongside the V0 (LC3) and VC3-15, reveals consistent patterns influenced by both cement and vaterite content (see Fig. 7 and Table S2). Reducing cement content from 45% to 40% leads to longer reaction duration, delayed peak time, lower peak amplitude, and a slight reduction in the peak integral. These shifts reflect slower and more diffuse aluminate hydration due to reduced clinker availability.

Similarly, increasing vaterite content at constant cement levels causes a delay in peak time, longer reaction duration, and reduced peak amplitude. However, unlike earlier results from the VC3 series (5–15% vaterite, constant MK content), the peak integral in the C45/C40 series remains relatively stable (Table S2). This deviation is likely due to the concurrent reduction in metakaolin content as vaterite increases. Since metakaolin is the main source of reactive alumina, its reduction partially offsets the expected effect of vaterite, thereby moderating the total heat release associated with the aluminate reaction.

In summary, both decreasing cement content and increasing vaterite content contribute to a broader, delayed, and less intense aluminate hydration peak. Where the range denotes the duration of the aluminate peak, the integral represents the total heat released during the aluminate reaction, the peak time marks the moment of maximum heat flow, and the amplitude reflects the peak intensity of the aluminate reaction.

Compressive strength performance

Figure 8 compares the compressive strength of LC3 mortar with three other calcined clay-based mortars containing calcite or vaterite, or both. The compressive strength of the LC3 mortar as the control mixture approximately lies within the range reported in previous studies for LC_3 systems containing 50% clinker and with 2:1 MK/calcite ratio[66–68]. At very early ages (1 day), all vaterite blended systems exhibited significantly lower strength than LC3counterparts. Contrary to expectations and previous findings[19], increasing the vaterite

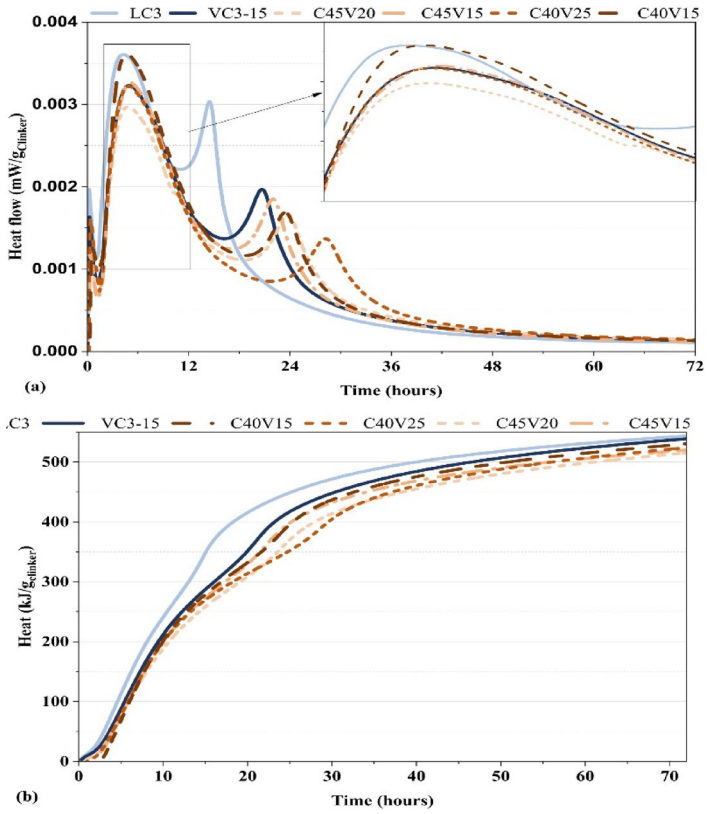

Fig. 7. Isothermal calorimetry results of the paste mixtures, normalized by clinker content: (**a**) normalized heat flow during hydration, (**b**) cumulative heat release.

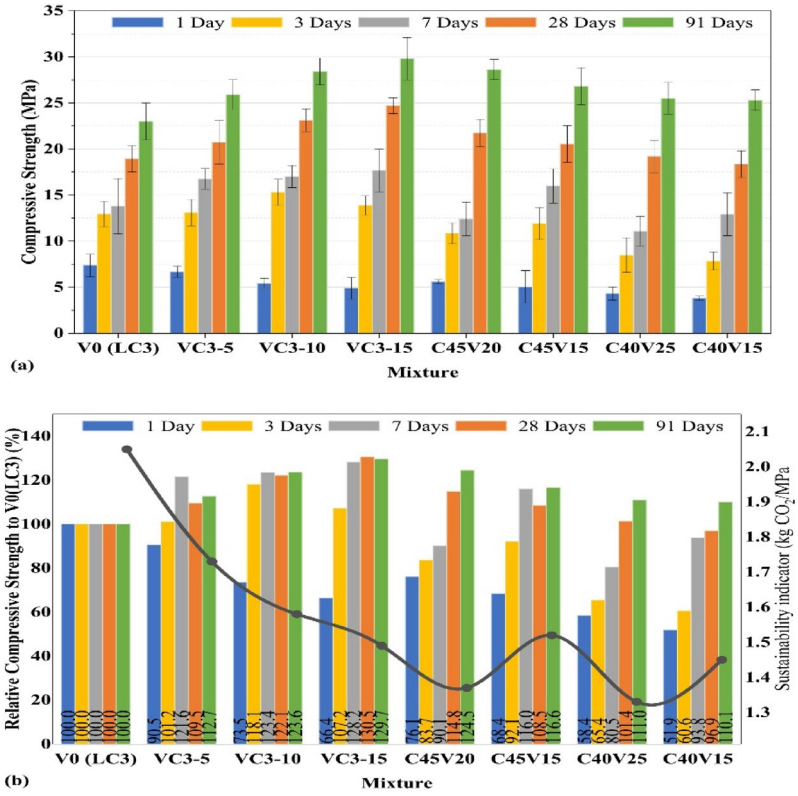

Fig. 8. Compressive strength of mortars: (up) at different curing ages; (down) normalized to the LC3 compressive strength and sustainability indicator at final curing age.

content negatively affected early strength development. Among the factors that may account for this divergent behavior, the specific surface area is particularly noteworthy. In the cited study[19], vaterite was reported to exhibit a specific surface area of 65.72 m^2/g, substantially higher than the value of 7.52 m^2/g determined in the present work. It is important to emphasize that the surface area of vaterite reported in the present work is consistent with values described in previous studies, as discussed in Sect. "Characterization of the synthesized vaterite". Some of these investigations[69] have identified elliptical vaterite, which exhibits significantly higher reactivity than its spherical counterpart, yet with a specific surface area of 27.21 m^2/g, less than half of the value reported in the aforementioned reference.

However, as curing progressed, a positive trend emerged: long-term compressive strength (28–91 days) improved with higher vaterite content. The VC3-15 mixture (with 15% vaterite) achieved the highest strength among the alternative binders. At 28 days, the strength of vaterite-based mortars ranged between 96% and 130% of the LC3 reference. By 91 days, these values increased to 112–130%, indicating substantial strength gains over time despite vaterite's lower specific surface area compared to calcite.

This time-dependent strength evolution highlights the complex role of vaterite in cementitious systems. The clear divergence between early-age and late-age performance suggests that hydration kinetics and microstructural development in vaterite-containing mortars may differ from those in conventional LC3. These findings underline the need for further investigation into the underlying mechanisms governing strength development in such systems.

The aim of this study was to examine the behavior and properties of vaterite when employed as a substitute material within the binder system. For this purpose, LC3 was incorporated primarily as a reference in a single composition. A complete series of LC3 samples analogous to the vaterite-based mixtures was not produced. Moreover, the differences arising from particle size heterogeneity and the tendency of vaterite to agglomerate could not be mitigated[56] owing to its synthetic origin and the inability to apply further grinding without altering the polymorphic ratio. Furthermore, the difference observed between calcite and vaterite in the current study reinforces the evidence regarding the advantageous role of vaterite. Despite possessing a lower specific surface area, vaterite demonstrates greater reactivity than calcite over both medium- and long-term timescales. These combined physico-chemical specifications of vaterite highlights that polymorph effect is not only but the primary driver of the observed strength enhancement.

Given vaterite's distinct physical and chemical characteristics compared to conventional calcium carbonate (i.e., calcite), it may help compensate for the reduction in cement content in mortar formulations. Figure 8 also presents the compressive strength results for mixtures with reduced cement content. While the absence of low-clinker LC3 mixtures limits a direct isolation of the vaterite effect at lower levels, the results demonstrate that VC3 enables significant clinker reduction without sacrificing long-term strength relative to the LC3 baseline

strength in 50% with cement. In the 45% cement mix, the formulation with higher vaterite content (C45V20) achieved 124% of the compressive strength of the LC3 reference mortar. Similarly, in the 40% cement mixture, the highest vaterite content resulted in 116% of the LC3 strength.

These findings suggest that increasing vaterite content can mitigate the strength loss typically associated with lower cement usage. This illuminates vaterite's potential as a viable component in the development of more sustainable, low-clinker cementitious systems.

Zeta potential

Zeta potential measurements revealed significant differences in the surface charge behavior of vaterite and calcite under various ionic conditions, with important implications for early hydration in blended cement systems. Figure 9a illustrates titration curves of aqueous suspensions of calcite and vaterite with increasing concentrations of $CaCl_2$ and K_2SO_4. The selected environments were designed to replicate the pore solution chemistry typical of early-age hydration. Immediately following water addition, the rapid dissolution of gypsum and C_3A phases of clinker generates a high concentration of these specific ionic species.

Vaterite exhibited substantially higher positive zeta potential values, reaching over + 160 mV, compared to a maximum of approximately + 58 mV for calcite. This can be understood by assuming an increased adsorption of calcium ions, which drives the zeta potential toward increasingly positive values. This finding suggests a much stronger affinity of vaterite for Ca^{2+} ions and suggests more intense adsorption from the pore solution.

In sulfate-rich environments (K_2SO_4), both carbonates initially showed a decrease in zeta potential due to SO_4^{2-} adsorption. This drop occurred more rapidly and to a lesser degree in calcite, while vaterite displayed a slower yet more significant decline, indicating a greater sulfate adsorption capacity. As titration advanced, the zeta potential of vaterite not only recovered but eventually surpassed that of calcite, thereby reflecting a potentially higher affinity for sulfate ions as well. This dual interaction with both sulfate and calcium ions suggests that vaterite may act as a temporary sink for essential reactants involved in ettringite formation.

The initially faster changes observed in calcite compared to vaterite—both the increase in zeta potential in the presence of calcium chloride and its decrease in the presence of potassium sulfate—can be attributed to differences in particle size (mainly due to the observed agglomeration of the vaterite particles), which initially

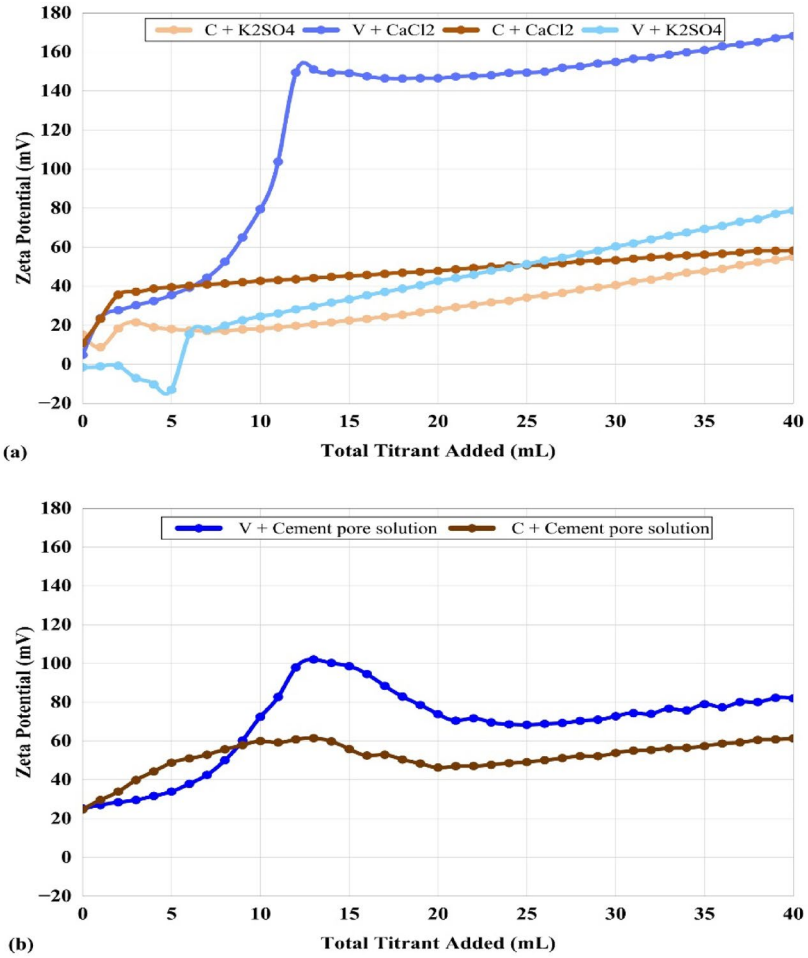

Fig. 9. Zeta potential of vaterite (V) and calcite (C) in: (**a**) 1 M calcium chloride ($CaCl_2$) or potassium sulfate (K_2SO_4) solutions, and (**b**) OPC (Cem I) pore solution at water-to-cement ratio (w/c) ca. 0.5.

promote more efficient adsorption processes on calcite. When tested in simulated cement pore solution, similar results were observed, and vaterite initially showed lower zeta potential values than calcite, likely due to its coarser particle size, which delays early ion adsorption. However, over time, vaterite's zeta potential steadily increased and ultimately surpassed that of calcite by approximately 20 mV, reflecting its greater capacity for sustained ion adsorption.

These trends provide a plausible basis for explaining the macroscopic observations: the strong and prolonged adsorption of Ca^{2+} and SO_4^{2-} by vaterite reduces their immediate availability for hydration reactions. Given that vaterite's dissolution rate reduced as its particle size increased[70], On the other hand, As demonstrated by the Fig. 9b in simulated pore solution (pH ≈ 13), vaterite exhibits a significantly higher positive surface charge (≈ 100 mV) than calcite (≈ 60 mV). This elevated potential indicates a superior capacity for the specific adsorption and sequestration of multivalent cations, particularly Ca^{2+}. By effectively trapping these essential ions on its surface, vaterite reduces their chemical activity in the aqueous phase during the first few hours of hydration. This sequestration temporarily and the delayed release of these ions limits early ettringite formation and C–S–H gel development. Consequently, setting is delayed and early-age strength is reduced. These findings further highlighting the influence of carbonate polymorph and particle characteristics on early hydration kinetics.

While the zeta potential trends in simplified aqueous environments provide a strong theoretical basis for the observed delay in hydration, it is acknowledged that the complex ionic competition and high solid-to-liquid ratios in actual VC3 pastes may influence the magnitude of these surface interactions. Nonetheless, the correlation between surface charge development and the prolonged induction period remains a compelling explanation for the observed behavior.

Phase assemblage

A qualitative evaluation of the XRD patterns using EVA provided a first indication of the main hydration trends in the LC3 and VC3s systems (Fig. 10). The evolution of the amorphous content, quantified using a 10 wt% corundum internal standard via TOPAS, reveals a distinct hydration pathway for the calcite and vaterite systems. The amorphous fraction (Fig. 11), representing the C-(A)-S-H gel and nanocrystalline hydration products, serves as an indicator of the development of the binding matrix. Figure 12 depicts the quantitative phase analysis and the corresponding graphs of calcium carbonates (Fig. 12a), ettringite (Fig. 12b), carboaluminates (Fig. 12c) and CH (Fig. 12d).

At 1 day, the V0 (LC3) reference exhibited a high amorphous fraction of 53.6%, whereas the vaterite-rich VC3-15 started significantly lower at 40.9%. This can also provide a basis for the lower 1-day compressive strength observed in all vaterite blended systems. This lag is entirely consistent with the longer induction period recorded in isothermal calorimetry which caused by the effect of the coarser particle size and secondary agglomeration of the synthesized vaterite on the kinetics of the hydration, which delays early ion release compared to the finer calcite.

At 91 days, it can be observed that the amorphous content in the V0 (LC3) reference gradually declined. This trend is interpreted as the progressive "mineralogical ripening" or crystallization of early-age metastable amorphous precursors into the well-ordered crystalline phases detected by XRD, such as Mc and ettringite. In contrast, the vaterite series exhibited superior late-age stability and sustained reactivity. While VC3-5 followed the reference trend (according to the higher content of calcite compare to vaterite), VC3-10 and VC3-15 maintained robust amorphous levels of 55.0% and 50.8%, respectively, through 91 days.

This sustained amorphous presence is supplied by the more pronounced long-term consumption of CH in the vaterite mixtures (Fig. 12d). The higher solubility of vaterite (log K_{sp} = -7.8) compared to calcite (log K_{sp} = -8.4) a thermodynamic factor provides a higher chemical driving force for continued pozzolanic and carbonate

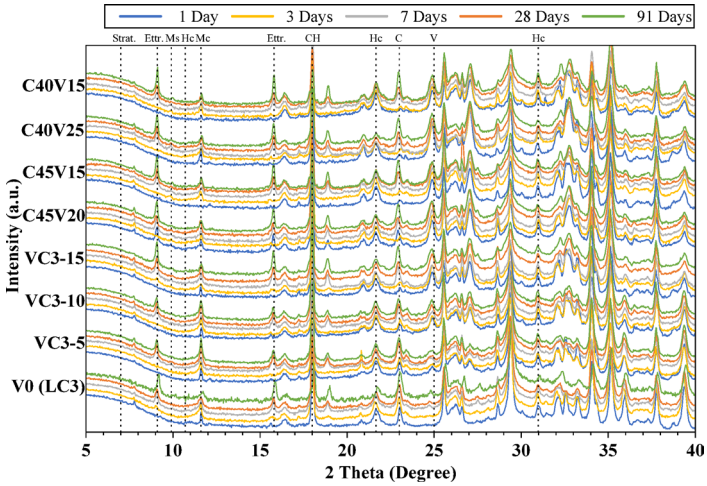

Fig. 10. XRD patterns of V0 (LC3) and VC3 pastes at 1, 3, 7, 28, and 91 days of curing. *Phase notation: Ettringite (Ettr.), Strätlingite (Strät.), Hemicarboaluminate (Hc), Monocarboaluminate (Mc), and Portlandite (CH).

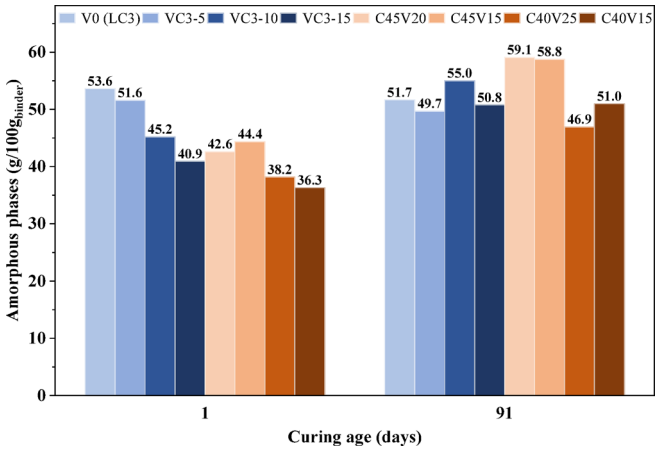

Fig. 11. XRD quantitative phase analysis of the content of amorphous phases in the mixtures at 1 and 91 curing days.

reactions at later ages[19]. This allows the VC3-15 system to produce more amorphous binder matrix, justifying the 130% strength gain relative to the reference at 91 days.

A general trend is observed where higher initial vaterite content leads to a reduction in amorphous phases at early ages compared to calcite-based mixtures. However, by 91 days of curing, the presence of vaterite consistently contributes to an increase in amorphous content across all binder types even mixtures with lower cement content.

In the LC3 mixture (V0), Hc was already visible from the earliest age, while no ettringite could be detected at 1 day. Ettringite formed between 1 and 3 days, and then increased at later curing ages. At later age, Mc became more evident and Hc was reduced by 91 days. In the VC3-5 and VC3-10 mixtures, no ettringite was observed at 1 and 3 days, whereas Hc was present at both ages and traces of monocarboaluminate appeared from 3 days onward. A pronounced ettringite peak developed at 7 days, followed by a slight reduction at 28 days. In VC3-5, the 28-day pattern also suggested an increase in monocarboaluminate.

In VC3-15, no ettringite was identified at 1 day, but Hc was already present, together with slight vaterite consumption which shows lower hydration products that align with the compressive strength results at 1-day curing. A small ettringite signal appeared at 3 days, and at 7 days, a much more intense ettringite signal was observed and Mc formation became apparent. At 91 days VC3-15 showed the largest ettringite content in the series, with both mono and Hc clearly present. Overall, these qualitative observations pointed to a general evolution of ettringite, with an initial formation peak between 3 and 7 days, and a secondary increase at 91 days, particularly evident in the vaterite rich mixture.

The quantitative phase analysis in Fig. 12 confirm these qualitative trends and allow a more detailed comparison between V0 (LC3) and the equivalent vaterite containing VC3-15 mixture. Ettringite is not detected at 1 day in any of the pastes, but in V0 it already reaches about 4.1 g/100g$_{binder}$ at 3 days and 5.4 g/100g$_{binder}$ at 7 days, and reaches to 9.9 g/100g$_{binder}$ at 91 days. In the VC3 systems, AFt formation is clearly delayed. VC3-15 shows an intermediate behavior, with a small AFt content already at 3 days (2.0 g/100g$_{binder}$), a pronounced peak at 7 days (7.9 g/100g$_{binder}$), and the highest late age AFt content at 91 days (12.8 g/100g$_{binder}$). This AFt evolution is consistent with the calorimetric results, where LC3 exhibits an earlier and sharper aluminate peak, while the VC3 mixtures, especially VC3-15, display a delayed but more extended aluminate reaction, and it also agrees with the SEM images that show scarce ettringite at 1 day and abundant needle like AFt at later ages in vaterite rich systems. Although vaterite promoted substantial AFt precipitation over time by reaching about 13 g/100g$_{binder}$ at 91 days, its stronger ion adsorption capacity delayed ion availability in the pore solution and extended the duration of AFt development, as ionic equilibrium gradually allowed the adsorbed ions to be released. Calcite in contrast provided more efficient nucleation sites for ettringite[16,71,72], explaining the faster early hydration and setting observed in LC3. This interpretation is supported by zeta potential measurements discussed before, indicating stronger adsorption (in practical terms, a sequestration) of calcium and sulfate ions on vaterite surfaces than calcite's. These results align with the longer setting times and delayed aluminate peaks recorded in isothermal calorimetry. The calorimetric aluminate peak, associated with the C_3A–gypsum reaction, occurred approximately six hours later in vaterite-rich binders, and its amplitude decreased with increasing vaterite content, confirming slower but sustained AFt formation. The slowdown in ettringite production at 28 days and its subsequent resumption are more prominent in VC3 samples than in analogous LC3 samples (Fig. 12b). This irregular crystallization of ettringite is due to the availability of sulfates: the gradual transformation of Hc (with the capacity to adsorb sulfate anions) into Mc (unable to retain sulfate for structural reasons) releases sulfate into the solution and allows the crystallization of new quantities of ettringite, in accordance with the work by Zunino[38,39]. In the case of VC3 mixtures, in addition, the balance of ions adsorbed in vaterite, including sulfate, shifts in the direction of releasing greater amounts of sulfates as vaterite reacts and dissolves, causing a much more marked spike in ettringite production (from 28 to 91 days).

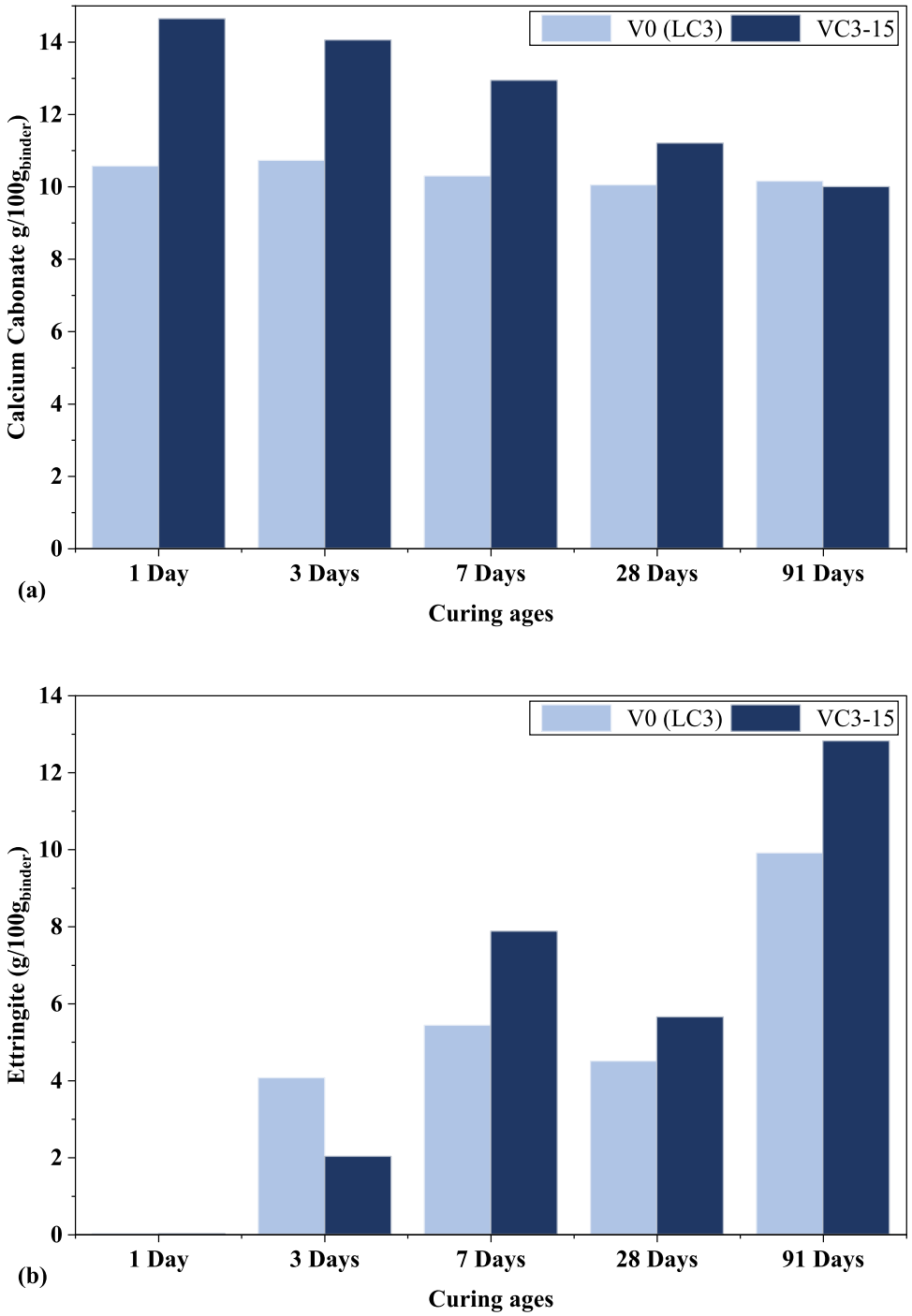

Fig. 12. XRD quantitative phase analysis of the V0 (LC3) andVC3-15 paste samples at 1, 3, 7, 28 and 91 curing days: (**a**) Calcium Carbonates, (**b**) Ettringite, (**c**) Carboaluminates, (**d**) Portlandite.

The behavior of the carbonate phases further differentiates the systems. In V0 (LC3), calcite remains close to 9–11 g/100g$_{binder}$ at all curing ages, with only minor fluctuations, indicating that calcite promoted the hydration and better compressive strength at 1 day. In contrast, the vaterite content in VC3-15 decreases from about 14.7 g/100g$_{binder}$ at 1 day to around 10 g/100g$_{binder}$ at 91 days, corresponding to a dissolution of more than 45% of the initial vaterite, in comparison to roughly 40% consumption of the initial calcite. This progressive vaterite consumption is consistent with the compressive strength results, which show stronger long term carbonate related reactions in the vaterite rich mixtures.

The evolution of carboaluminate phases confirms that Hc forms early and gradually converts into monocarboaluminate. In V0, Hc contents decrease from around 1.6 g/100g$_{binder}$ at 1 day to about 0.5 g/100g$_{binder}$ at 91 days, while Mc increases from an initially low value to nearly 2.2 g/100g$_{binder}$ at 91 days. In VC3-5 and

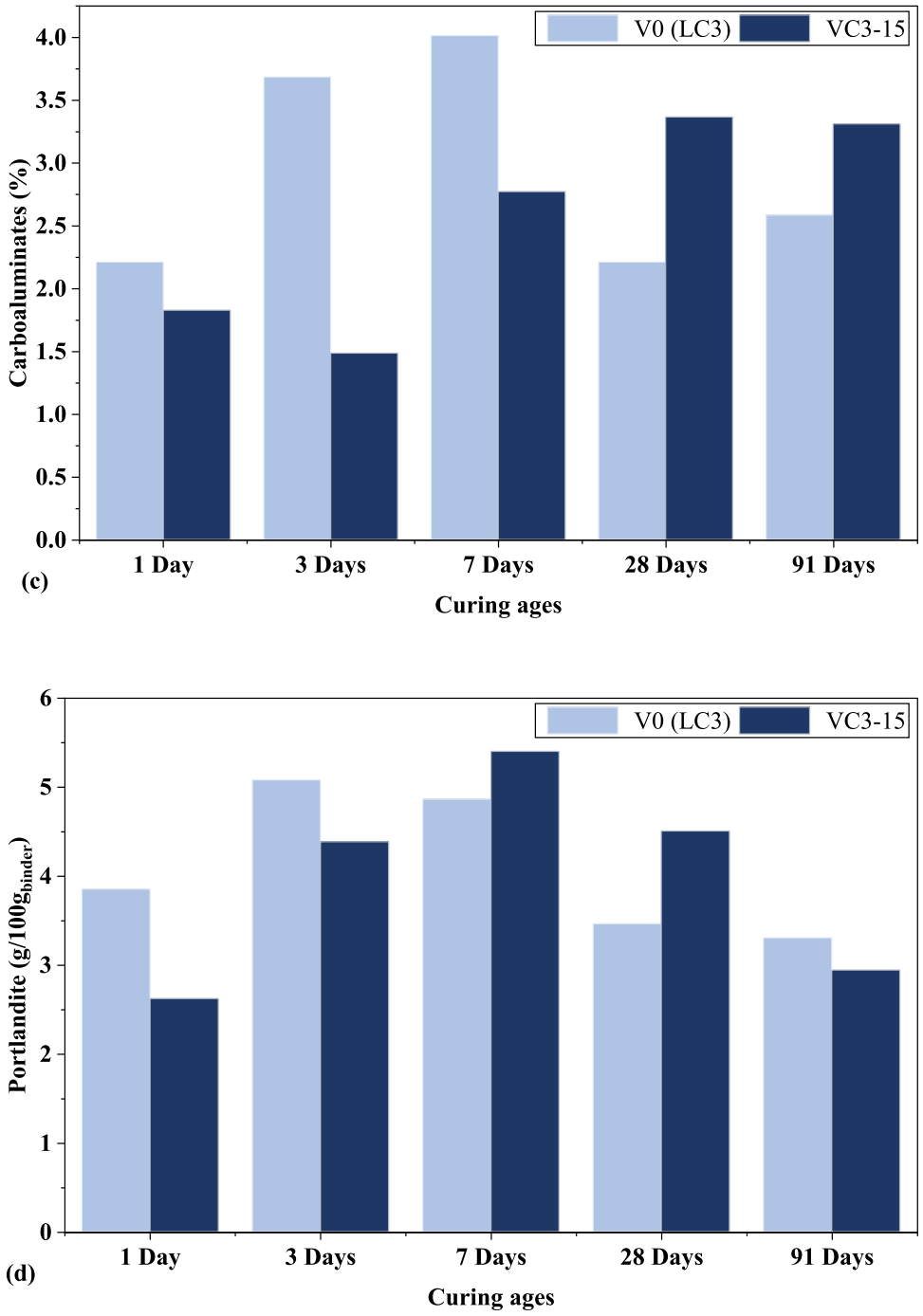

Fig. 12. (continued)

VC3-10, Hc is also present at 1 and 3 days, with Mc appearing or increasing from 3 days onward, in agreement with the qualitative observations. VC3-15 behaves similarly but with higher absolute levels of AFm at later ages. Hc remains clearly detectable up to 91 days, and Mc rises from undetectable at 1 day to about 1.8 g/100g$_{binder}$ at 91 days. When Hc and Mc are considered together, the total carboaluminate content increases with curing in all mixtures, more markedly in VC3-15, which gradually increased to about 3.5 g/100g$_{binder}$ at 91 days. This reflects sustained alumina–carbonate interaction driven by vaterite dissolution and is consistent with the delayed but robust aluminate peak recorded in isothermal calorimetry. This trend is consistent with the findings of Li et al.[19]

Compared to some previous studies, the percentages of carboaluminates are lower[38,39], and the crystallinity of the Hc is less evident, as shown by the low intensity of the peak at 10.78° 2-theta (highlighted in some studies as outstanding diffraction peak). In the present work, the assessment of the Hc has been related to the peaks at 21.66, 30.98, and 44.34° 2-theta, highlighted as the most intense diffraction lines according to PDF file 41–0221.

Considering also the moderate mechanical strengths, a low-reactivity metakaolin could be at the origin of these observations, which affected both the VC3 series and the LC3 mixture.

CH evolution links XRD with mechanical performance. In V0 (LC3), CH increases from about 3.8 g/100g_{binder} at 1 day to a maximum of roughly 4.8–5 g/100g_{binder} at 3–7 days, then decreases to around 3.4 g/100g_{binder} at 28 days and 3.3 g/100g_{binder} at 91 days, in line with the typical sequence of clinker hydration followed by pozzolanic and carbonate reactions in LC3. The initial increase is associated with the C_3S hydration and the consumption of CH accounts for the pozzolanic reaction of the MK. The remaining CH indicated that long-term hydration reactions might be expected, in line with the literature[38,39]. The VC3 mixtures show similar early CH levels but a more pronounced long-term consumption, especially in VC3-15. In that mixture, CH increases from 2.6 g/100g_{binder} at 1 day to 5.4 g/100g_{binder} at 7 days and further to 4.5 g/100g_{binder} and 2.9 g/100g_{binder} at 28 and 91 days, respectively, corresponding to a larger relative CH loss than in LC3. This consumption of CH can be considered as an indication of the sustained reactivity at long-term of the vaterite-bearing mixtures. Altogether, the quantitative XRD results show that replacing calcite with vaterite delays early AFt precipitation and CH consumption but enhances long term vaterite dissolution, AFt and carboaluminate formation and CH depletion, which explains the combination of slower early hydration and improved medium- and long-term performance observed in the VC3 systems.

The QPA results (Fig. 13) of the samples with lower clinker proportion, support the interpretation from isothermal calorimetry that reducing clinker content, together with increasing vaterite proportions, shifts the aluminate reaction more to later times. In the C45 and C40 binders, ettringite was either absent or detectable only in small amounts at 3 days (1.1–2.2 g/100g_{binder}), whereas LC3 and the higher-cement VC3 mixtures had already formed appreciable AFt at the same age. With continued curing, however, the reduced-OPC systems developed substantially higher AFt contents, consistent with the broadened and delayed aluminate peak observed in calorimetry. This indicates that lower cement availability and stronger ion adsorption on vaterite surfaces not only delay early ettringite precipitation but also extend the AFt formation window toward later ages.

The evolution of the carbonate phases reinforces this chemical consumption model. Rather than a mere loss of material, vaterite was progressively consumed through dissolution-reprecipitation mechanisms and partial polymorphic transformation into calcite. In the C45V20 and C40V15 binders, crystalline vaterite content decreased by more than 65% (from 19.7 to 6.4 g/100g_{binder}) and 70% (from 17.6 to 4.8 g/100g_{binder}), respectively. This reduction represents the stoichiometric redistribution of carbonate into the hydrated matrix. A significant portion of this reduced mass is accounted for by the precipitation of carboaluminate phases (Hc and Mc), while the remaining balance is attributed to the incorporation of carbonate ions into the amorphous C-(A)-S-H gel or the formation of poorly crystalline AFm phases[12]. This is supported by EDS analysis, which reveals vaterite and calcite surfaces intermixed with C-(A)-S-H gel, as well as vaterite particles infilled with AFm and C-(A)-S-H products[19].

Also, Zhou et al.[73] reported that in alkaline environments, these phases are often poorly crystalline and therefore may not always be detectable by XRD. By utilizing ^{27}Al Magic Angle Spinning Nuclear Magnetic Resonance (MAS NMR) to track octahedrally coordinated aluminum in AFm phases (such as Ms and Mc) they provided a theoretical explanation for the XRD deficit in detecting the complete percentage of the carboaluminates.

This interpretation ensures a consistent mass balance, where the total $CaCO_3$ introduced is conserved within the newly formed hydration products, as corroborated by the corresponding increase in chemically bound water observed in TGA.

This sustained dissolution aligns with the stronger long-term carbonate-related reactions observed in the low-OPC systems and correlates with their progressively increasing compressive strength.

CH evolution further clarifies the hydration mechanism. The remaining CH content at final age decreased systematically with reducing clinker content: from 5.3 → 1.8 g/100g_{binder} in C45V20 (ca. 70% reduction), 4.3 → 0.9 g/100g_{binder} in C45V15 (ca. 80% reduction), and from 6 → 1 g/100g_{binder} in C40V15 (ca. 87% reduction). In C40V25, CH dropped from 2.9 g/100g_{binder} to approximately 0.3 g/100g_{binder} by 28 days (ca. 92% reduction). These reductions are fully consistent with TGA, where the CH-associated mass-loss peak nearly disappears in the 40% OPC binders, confirming very advanced pozzolanic and carbonate reactions. The combined trends of delayed AFt formation, sustained vaterite dissolution, and strong long-term CH consumption explain the slower early hydration but the pronounced medium- and late-age reactivity characteristic of these low-clinker, vaterite-rich systems.

Figure 14, S2, S3, and S4 (Supplementary material) present the thermogravimetric analysis results, showing the evolution of ettringite and hydration products, CH, and calcium carbonate ($CaCO_3$), across different curing ages and binder compositions in the different mortar specimens. The onset temperature of each weight-loss event was determined from the DTG curve as the point where the derivative signal began to deviate from the baseline. The specific temperature intervals and the corresponding phase assignments used for the quantitative interpretation of these curves are summarized in Table 5. At early ages (1–3 days), vaterite blended mixtures exhibit significantly lower amounts of weight loss around 105 °C with 0.39–0.48% compared to the LC3 mortar with 0.47–0.55%, consistent with weaker early AFt formation observed by XRD. This reduction correlates with their reduced early-age compressive strength.

* Vaterite decomposition range experimentally verified by TGA of the raw material source.

In the OPC mixtures, the CH content increases steadily over time, reflecting the continuous hydration of clinker phases[18]. In contrast, the blended systems follow a different trend: CH content rises during the early stages (typically between 1 and 3 days), even up to 22% more than initial amount and then decreases. This reduction is attributed to pozzolanic reactions between CH and the alumina from metakaolin, as well as with reactive carbonate phases, leading to the formation of C-(A)-S-H and carboaluminate phases (Eq. 1)[74]. The concurrent increase in bound water content (within the 105–400 °C) observed in the blended mixtures (from

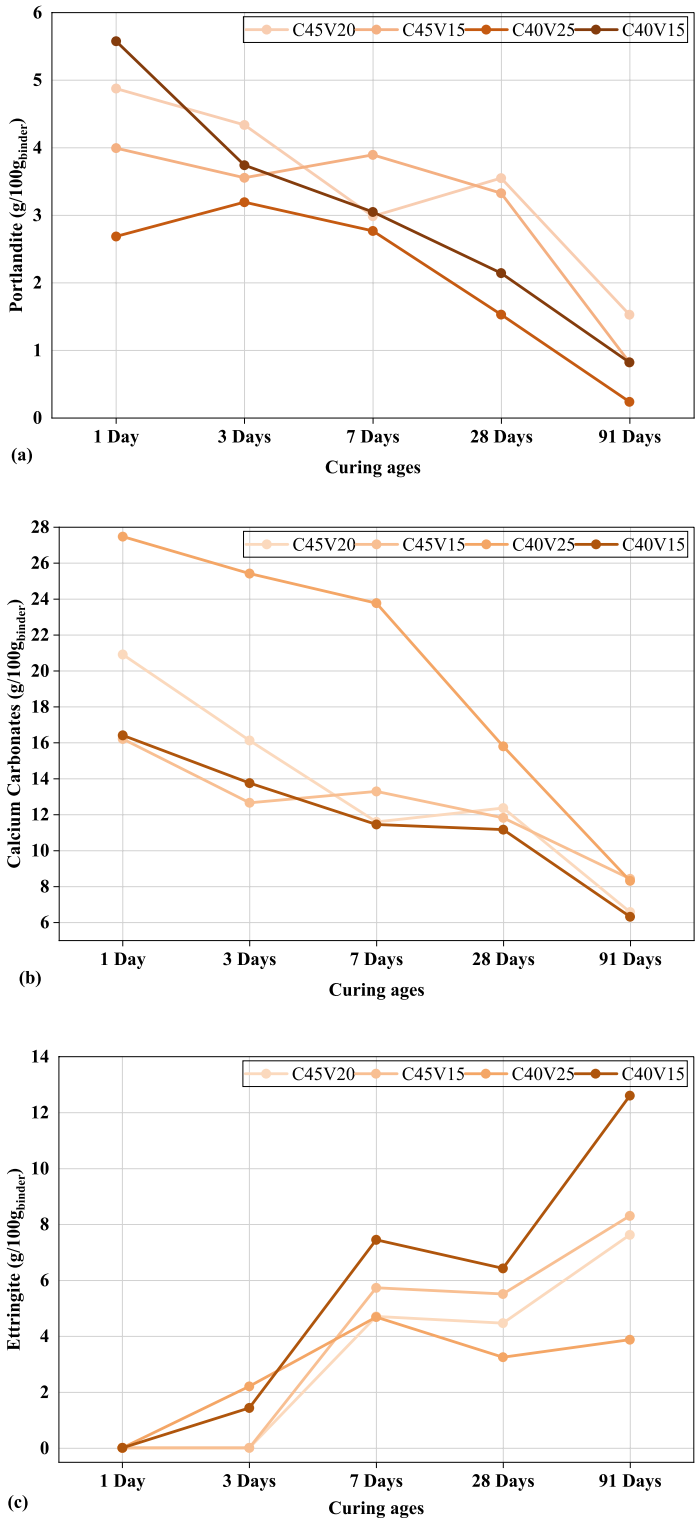

Fig. 13. XRD quantitative phase analysis of the C45V20, C45V15, C40V25, and C40V15 pastes at 1, 3, 7, 28, and 91 days of curing: (**a**) Portlandite, (**b**) Calcium Carbonates (Vaterite), (**c**) Ettringite.

less than 2% after 1 day of curing to more than 4% after 91 days) supports this behavior and confirms the continued hydration and pozzolanic activity throughout curing.

The evolution of CH content (Fig. 15), identified by mass loss in the 420–480 °C range, aligns well with the hydration trends observed in calorimetry and setting time results. All blended systems showed an initial increase in CH content between 1 and 3 days, indicating active hydration of C_3S and C_2S. However, the rate and extent of subsequent CH consumption varied across the mixtures, offering insights into their pozzolanic

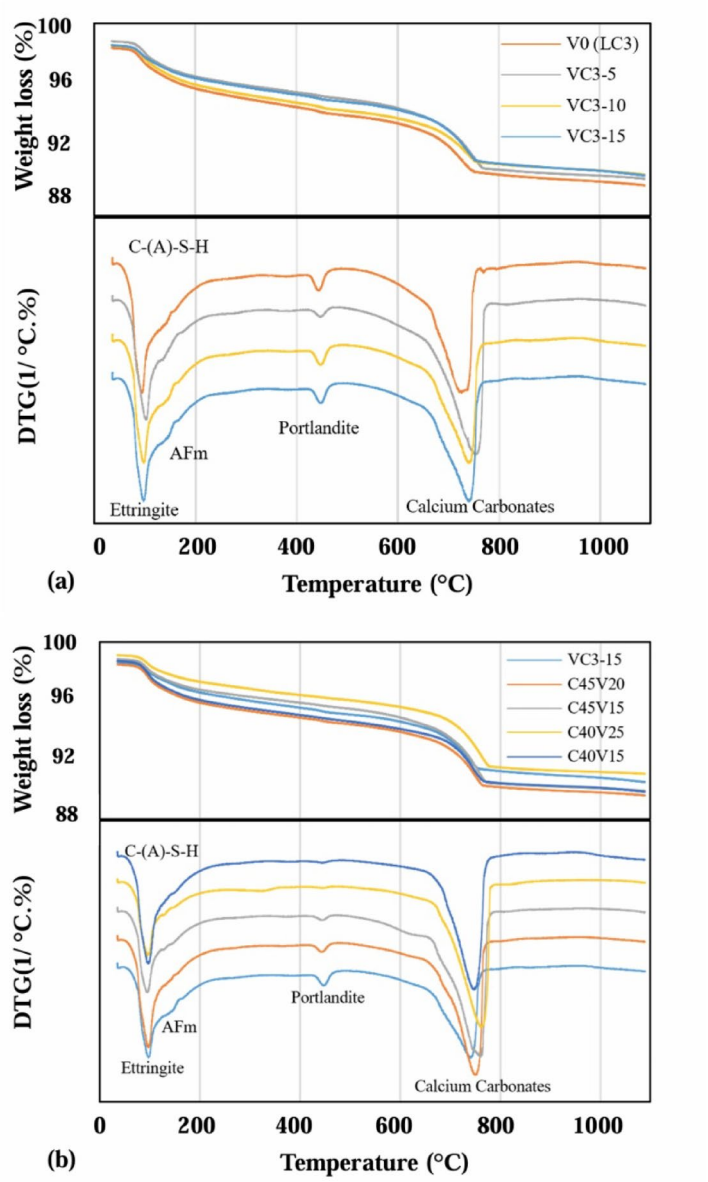

Fig. 14. Thermogravimetric analysis (weight loss%) and differential thermogravimetric (DTG) curves at 91 days of mortar samples: (**a**) V0 (LC3), VC3-5, VC3-10, and VC3-15, (**b**) V0 (LC3), VC3-15, C45V20, C45V15, C40V25, and C40V15.

Temperature range (°C)	Assigned phase / event	Potential overlaps
40–120	Ettringite (AFt) dehydration	C-S-H
120–200	AFm (Hc/Mc) dehydration	C-S-H, Gypsum
400–480	Portlandite (CH) dehydroxylation	None (Isolated)
600–800	Carbonate ($CaCO_3$) decomposition	Vaterite*, Calcite

Table 5. Temperature intervals and phase assignments via TGA/DTG[55].

reactivity. In V0 (LC3) and VC3-5, where calcite is the dominant carbonate source, CH content began to decline after 3 days, consistent with the onset of pozzolanic consumption and carboaluminate formation. TGA results showed that weight loss in the 420–480 °C range in these 2 samples reached 0.51–0.58% while after 91 days they declined to less than 0.35%This aligns with the sharper aluminate peaks in the isothermal calorimetry tests and shorter setting times, as previously discussed. Portlandite quantified by multiplying the water mass loss in the 420–480 °C range by the stoichiometric factor of 4.11 (Molecular Weight of $Ca(OH)_2$/ Molecular Weight of

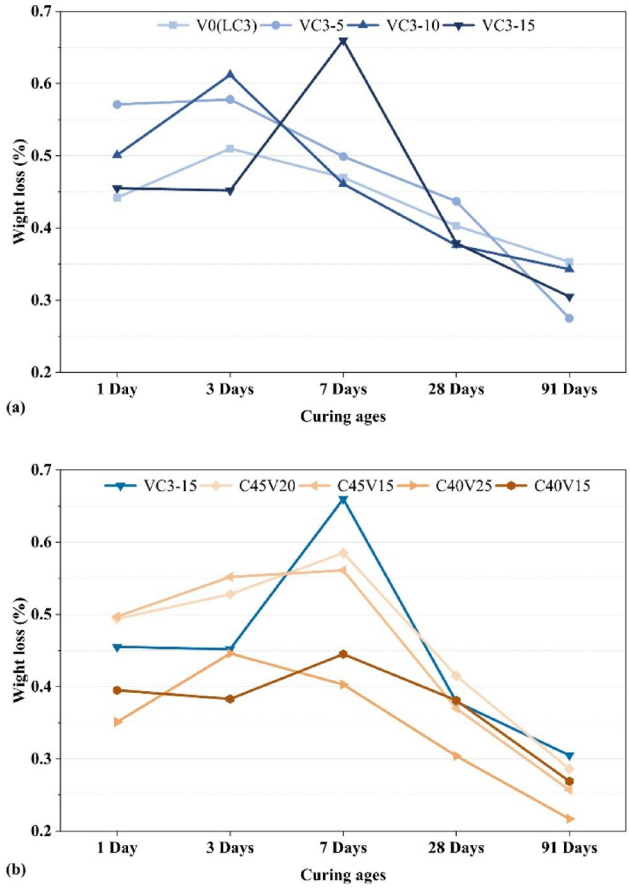

Fig. 15. Evolution of weight loss between 420–480 °C (ascribed to the portlandite content) over time in the mortar samples: (**a**) V0 (LC3), VC3-5, VC3-10, and VC3-15, (**b**) VC3-15, C45V20, C45V15, C40V25, and C40V15.

H_2O). Although the absolute values of are not exactly equal to values from XRD—due to the inherent differences between thermal and diffraction-based measurements—the developmental trends align remarkably well with the QPA results.

VC3-10 showed intermediate behavior. While CH content increased notably between days 1 and 3 (up to 0.6%), its consumption began later than in V0 (LC3) or VC3-5. This delay is attributed to the reduced calcite content and the higher proportion of vaterite particles. The delayed reactivity is consistent with the lower aluminate peak intensity observed in calorimetry and the extended setting times recorded in VC3-10 and VC3-15.

In VC3-15, which contains no calcite, CH content rose by ca. 40% from the initial amount by day 7 (reaching a peak) before decreasing ca. 60% from that peak. This further confirms vaterite's delayed but sustained pozzolanic activity. Similar behavior was observed in lower-OPC mixtures such as C45V20 and C40V25, where vaterite is the sole carbonate phase. At 91 days. The differential thermogravimetry (DTG) signal corresponding to CH (420–480 °C) nearly disappears in the 40% OPC mixtures, and no measurable mass loss is detected in this range (see Fig. 14b), suggesting near-complete CH consumption through pozzolanic and carbonate-related reactions.

Although the vaterite-containing mixtures perform with lower compressive strength at early curing ages, vaterite-rich mixtures (VC3-10 and VC3-15) showed significant strength gains by 28 days despite lower hydration product content. By 91 days, vaterite-rich mixtures reached 29.8 MPa, underscoring the importance of long-term curing in realizing the full performance potential of vaterite-containing binders.

CH, formed during the hydration of calcium silicate phases (C_2S and C_3S) in OPC, reacts with metakaolin to yield C-A-S-H and calcium aluminate hydrate (C_4AH_{13}) phases (Eq. 1)[74]. While in the presence of sulfate, CH reacts with metakaolin and calcium carbonates to form Hc (Eq. 2 and Eq. 3) after sulfate depletion[75].

The progressive reduction in CH with increasing vaterite content reflects the enhanced long-term reactivity of vaterite compared to calcite. These results confirm that the binder composition, particularly the type and particle size of carbonate source, strongly influences hydration product evolution and strength development. Through mechanisms such as pore refinement[19,63], continued pozzolanic activity, and delayed but sustained reactivity, VC3 systems can achieve higher long-term mechanical performance than that of LC3[19,65].

Microstructural examination

Figure 16 presents SEM images of VC3-15 (Fig. 16a-f) and V0 (LC3) (Fig. 16g-l) mortars at various curing ages (1, 3, 7, 28, and 91 days) and Fig. 17a-f the images of VC3-15 at 7 curing days, highlighting the progression of microstructural and compound precipitation development over time. Both systems exhibit increasingly dense matrices as curing advances, with the VC3-15 mortar showing a noticeably more compact microstructure and more consumed CH (more porous structure of CH), as can be seen in Fig. 16f, compared to V0 (LC3) by 91 days in Fig. 16l.

In the 1-day LC3 (Fig. 16g), nascent ettringite develops only marginally and although it is not detectable by other techniques at early stages, a slight trace of its precipitation can be observed, characterized by the presence of needle-like crystals. These ettringite structures become more pronounced at later ages (Fig. 16i and j), indicating continuous precipitation. In contrast, ettringite were not observed in the 1-day VC3-15 sample (Fig. 16a); however, it becomes clearly detectable in Fig. 16c and e, and Fig. 16f, reflecting the delayed ettringite formation typical of vaterite-containing systems.

At 3 days, in Fig. 16b, VC3-15 samples display larger CH crystals compared to the smaller CH formations observed in Fig. 16h, in the LC3 specimens. This difference resulted from the distinct CH consumption behavior previously discussed, which attributes it to the unique characteristics of vaterite as the carbonate source, which is further supported by the zeta potential results. Additionally, the 7-day VC3-15 images (Figs. 16d and 17a, c, d and f) show undissolved and intact vaterite and/or CH particles, which are still identifiable at this stage. At later curing ages, these particles appear to be surrounded by well-developed ettringite needles (Fig. 16e), suggesting that the later consumption of vaterite favors the ettringite formation during the extended hydration period and starts to be consumed compared to the LC3 sample (Fig. 16k), which shows that the consumption of CH is in a more progressed state. These findings are fully consistent with the previously discussed results on zeta potential, isothermal calorimetry, and the evolution of mineralogical phases as identified by XRD and TGA, thereby providing a mechanistic explanation for the observed improvements in compressive strength with increasing curing age.

Figure 18 presents EDS elemental mapping of the VC3-15 mortar at 3 days, offering insights into the early-stage hydration mechanisms. Distinct zones rich in calcium in Fig. 18 (Ca mapping) confirm the presence of CH (plate-like hexagonal crystals), indicating active hydration. The sulfur distribution map in Fig. 18 (S mapping) reveals localized regions of early ettringite formation, characterized by fine particle nucleation, evidence that the precipitation of AFt phases has already commenced at this age.

The carbon mapping indicates the presence of residual spherical particles, attributed to undissolved vaterite (Fig. 19). This observation suggests that vaterite dissolution becomes more pronounced after 7 days, when it increasingly contributes to the hydration process, particularly through interactions with CH and alumina sources. At this stage, the formation of C–S–H and nascent ettringite is instrumental in early strength development, partially compensating for the lower 1-day compressive strength of the VC3-15 mortar compared to its LC3 counterpart.

Sustainability indicator

The simplified comparative indicator of the mortar in Fig. 8b indicates that the control blend LC3 recorded the highest carbon emission intensity of 2.016 kg CO_2/MPa. Incorporation of vaterite consistently lowered this value: VC3-5 at 1.762, VC3-10 at 1.581, and VC3-15 at 1.484 kg CO_2/MPa. These reductions arise from vaterite's negative sequestration footprint[19], which offsets emissions from OPC and other constituents.

Further OPC reduction yielded additional environmental gains. C45V20 achieved an indicator of 1.372 kg CO_2/MPa, representing a 32% decrease relative to V0 (LC3), while C45V15 registered 1.514. The lowest indicator, 1.345 kg CO_2/MPa, was observed for C40V25. Even C40V15 maintained a significant reduction at 1.462 kg CO_2/MPa. Overall, the vaterite replacement reduced embodied carbon intensity by up to 33%.

Conclusions

This study evaluated the performance of Vaterite Calcined Clay Cement as a sustainable alternative to conventional LC3 systems, focusing on hydration behavior, phase assemblage, microstructural evolution, and mechanical performance. The findings highlight the critical role of vaterite content in both fresh and hardened properties:

I. Physicochemical and Fresh-State Properties.

1. Surface charge behavior: Zeta potential measurements indicated that, despite its tendency to form agglomerates, vaterite has a higher ion adsorption capacity than calcite, particularly in calcium- and sulfate-rich environments. This reduces early ion availability, delaying early hydration and resulting in lower early-age strength.
2. Improved workability: The inclusion of vaterite enhances the flowability of calcined clay mortars compared to LC3. This is attributed to vaterite's spherical morphology. Flow-table results consistently show increasing flowability with higher vaterite content.
3. Extended setting: VC3 mortars exhibited longer setting times than LC3, primarily due to vaterite's slower dissolution rate and to the trend to agglomerate, yielding coarser particles. In low-cement formulations, higher vaterite content further extended setting times.

II. Hydration Kinetics and Phase Assemblage.

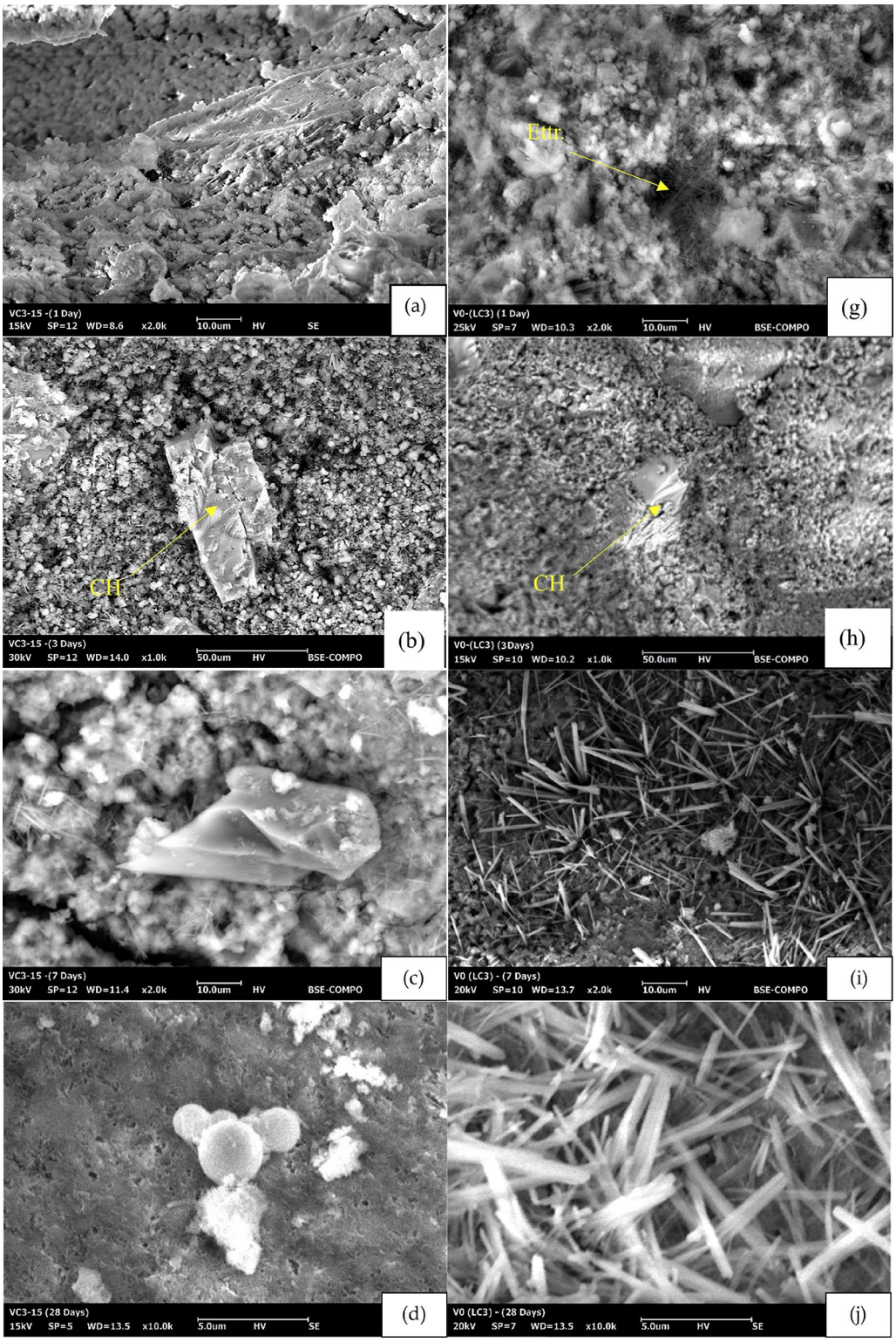

Fig. 16. SEM images showing microstructural development of VC3 mortar at different curing ages: (**a**) VC3-15, 1 day; (**b**) VC3-15, 3days; (**c**) VC3-15, 7days; (**d**) VC3-15, 28days; (**e**) VC3-15, 28days; (**f**) VC3-15, 91 days; (**g**) V0 (LC3), 1 day; (**h**) V0 (LC3), 3days; (**i**) V0 (LC3), 7days; (**j**) V0 (LC3), 28days; (**k**) V0 (LC3), 28days; (**l**) V0 (LC3), 91days. *Phase notation: CH; Portlandite, Ettr.; Ettringite.

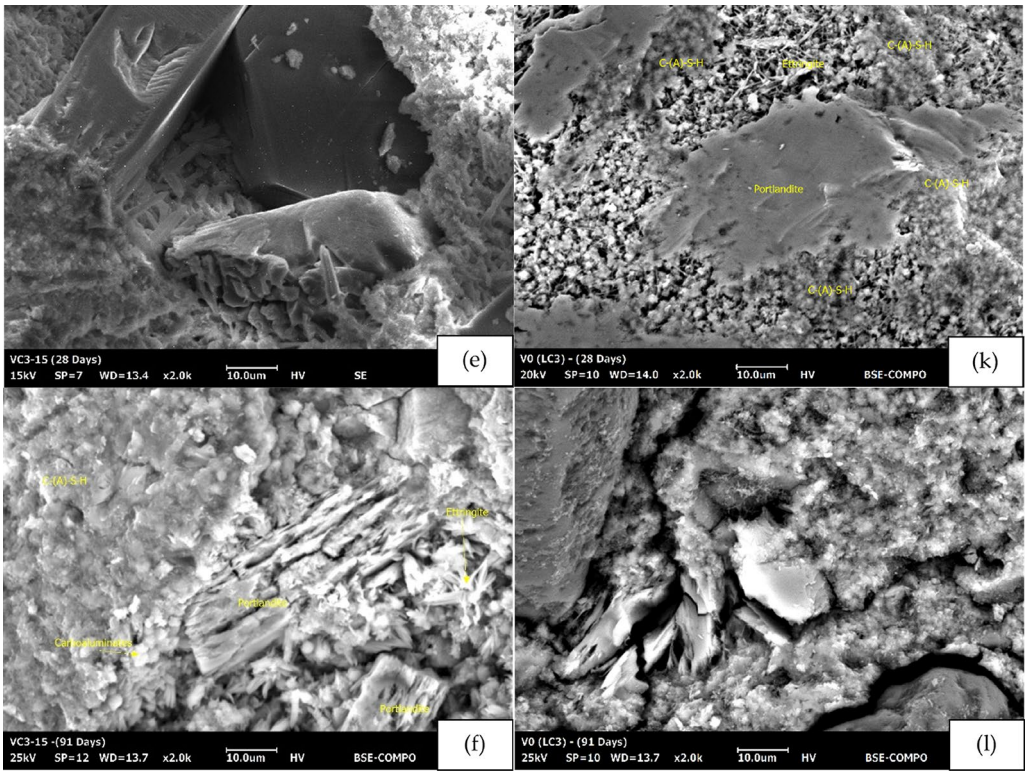

Fig. 16. (continued)

4. Modified hydration kinetics: Isothermal calorimetry revealed delayed and broadened aluminate peaks in VC3 mixtures, indicating slower but more sustained hydration reactions. The timing and intensity of these peaks were strongly influenced by vaterite dosage.
5. Phase Evolution: XRD and TGA analyses confirmed the progressive development of Portlandite consumption and forming carboaluminate phases (Hc and Mc) and etteringite. While the initial formation of hydration products are retarded in VC3 systems, it becomes more extensive over time (91 days) compared to LC3.
6. Prolonged Pozzolanic Activity: TGA results demonstrated extended CH consumption in VC3 mortars at later ages, suggesting that the vaterite-calcined clay interaction promotes continued pozzolanic reactivity and matrix densification.

III. Mechanical Performance and Microstructure.

7. Mechanical performance: VC3 mortars showed significant strength gains at later ages, reaching up to 130% of the LC3 reference at 91 days. They also outperformed LC3 in terms of long-term strength. Higher vaterite content was associated with greater final compressive strength.
8. Low-cement formulations: VC3 mortars with reduced cement content (40–45%) achieved long-term compressive strengths superior to the LC3 control under similar conditions, demonstrating the potential for cement reduction without compromising performance.
9. Microstructural evolution: SEM and EDS observations confirmed that the late-age strength gain is associated with a denser microstructural matrix resulting from sustained hydration and the growth of carboaluminate phases.

IV. Sustainability Indicators.

10. Sustainability: In a simplified comparison, vaterite incorporation significantly reduces the CO_2 emission intensity of mortars by up to 33% compared to LC3. This reduction was further improved with OPC reduction, demonstrating that vaterite can simultaneously reduce embodied carbon and maintain or even improve mechanical performance.

Although vaterite may retard early hydration, its positive impact on long-term strength development, along with its potential to reduce the environmental footprint, highlights its promise as a key component in sustainable, low-clinker cementitious systems. Its incorporation into calcined clay binder systems improves fresh-state properties and promotes favorable hydration and microstructural evolution over time. These benefits are highly dependent on vaterite content, and the performance observed in the VC3 formulation suggests that it is a technically viable and high-performing binder.

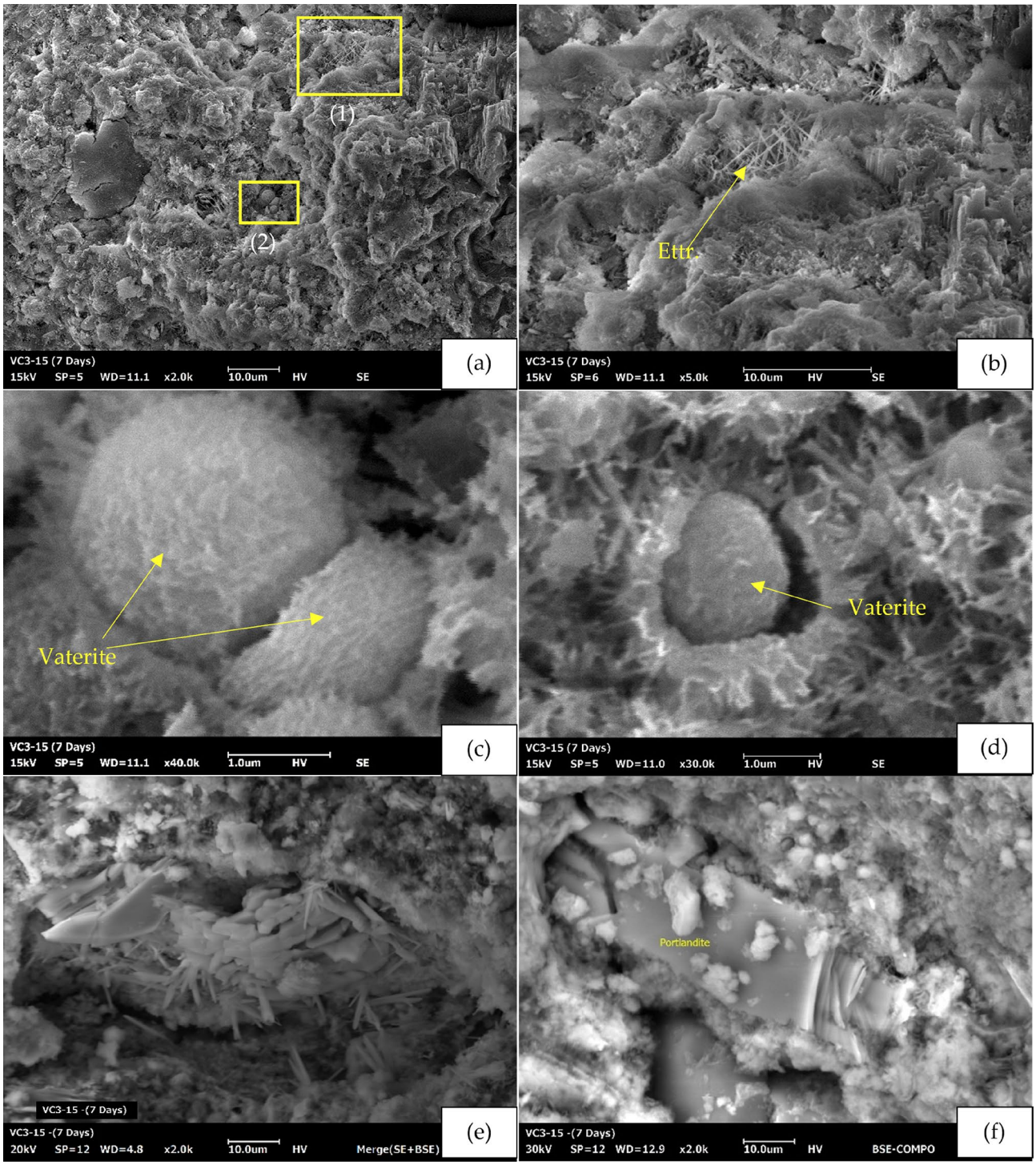

Fig. 17. SEM images of VC3-15 mixture at 7 days: (**a**)[1] nucleation of ettringite particles and[2] undissolved vaterite and, (**b**) magnification of area 1 and (**c**) magnification of area 2 indicated in image (**a**), (**d**) undissolved vaterite particle, (**e**) early precipitation of ettringite, and (**f**) intact portlandite.

However, to fully assess the applicability in sustainable construction and transition this technology to industrial application, further investigation into the material life cycle performance, rheology, and long-term durability is warranted.

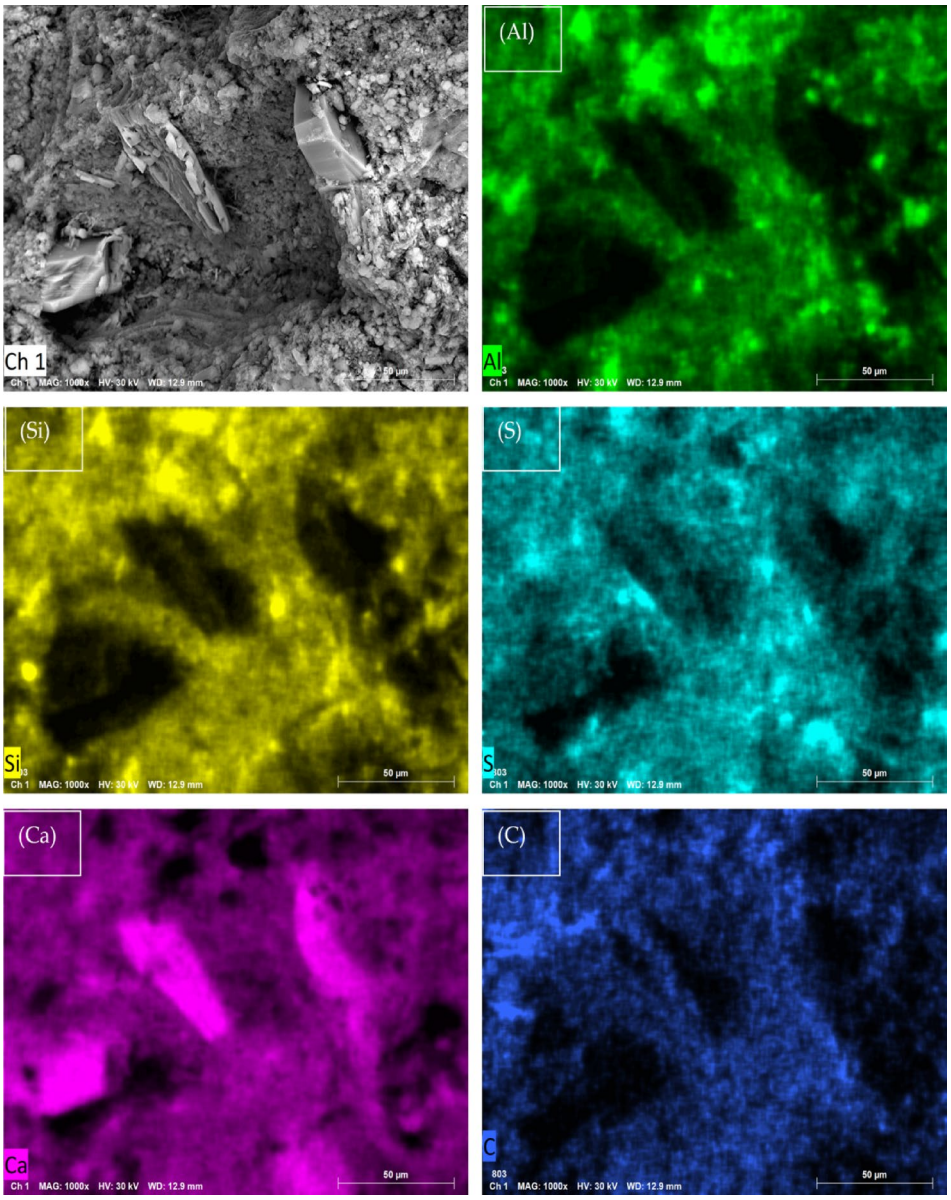

Fig. 18. Elemental mapping of the VC3-15 mortar at 3 days using EDS: (Al) Aluminum, (Si) Silicon, (S) Sulfur, (Ca) Calcium, and (C) Carbon.

Fig. 19. SEM image of the VC3-15 mortar sample associated with elemental mapping by EDS at 3 days: (Al) aluminum, (Si) silicon, (S) sulfur, (Ca) calcium, and (C) carbon.

Data availability

The datasets used and/or analysed during the current study available from the corresponding author on reasonable request.

Received: 4 February 2026; Accepted: 27 April 2026
Published online: 02 May 2026

References

1. Scrivener, K. L., John, V. M. & Gartner, E. M. Eco-efficient cements: Potential economically viable solutions for a low-CO2 cement-based materials industry. *Cem. Concr Res.* **114**, 2–26. https://doi.org/10.1016/j.cemconres.2018.03.015 (2018).
2. Lund, H. & Hvelplund, F. The economic crisis and sustainable development: The design of job creation strategies by use of concrete institutional economics. *Energy* **43**, 192–200. https://doi.org/10.1016/j.energy.2012.02.075 (2012).
3. Zheng, Y. et al. Effect of composite activator on hydration kinetics and micromechanical properties of alkali-activated slag. *Cem. Concr Compos.* **160**, 106047. https://doi.org/10.1016/j.cemconcomp.2025.106047 (2025).
4. Gartner, E. Industrially interesting approaches to low-CO2 cements. *Cem. Concr Res.* **34**, 1489–1498. https://doi.org/10.1016/j.cemconres.2004.01.021 (2004).
5. Miller, S. A., John, V. M., Pacca, S. A. & Horvath, A. Carbon dioxide reduction potential in the global cement industry by 2050. *Cem. Concr Res.* **114**, 115–124. https://doi.org/10.1016/j.cemconres.2017.08.026 (2018).
6. Lothenbach, B., Scrivener, K. & Hooton, R. D. Supplementary cementitious materials. *Cem. Concr Res.* **41**, 1244–1256. https://doi.org/10.1016/j.cemconres.2010.12.001 (2011).
7. Zheng, Y. et al. Development of high-performance phosphogypsum-based cementitious materials through CO2-assisted alkali activation. *Cem. Concr Compos.* **162**, 106144. https://doi.org/10.1016/j.cemconcomp.2025.106144 (2025).
8. Hamada, H. M. et al. Effect of silica fume on the properties of sustainable cement concrete. *J. Mater. Res. Technol.* **24**, 8887–8908. https://doi.org/10.1016/j.jmrt.2023.05.147 (2023).
9. Juenger, M. C. G., Snellings, R. & Bernal, S. A. Supplementary cementitious materials: New sources, characterization, and performance insights. *Cem. Concr Res.* **122**, 257–273. https://doi.org/10.1016/j.cemconres.2019.05.008 (2019).
10. Snellings, R., Suraneni, P. & Skibsted, J. Future and emerging supplementary cementitious materials. *Cem. Concr Res.* **171**, 107199. https://doi.org/10.1016/j.cemconres.2023.107199 (2023).
11. Schöler, A., Lothenbach, B., Winnefeld, F. & Zajac, M. Hydration of quaternary Portland cement blends containing blast-furnace slag, siliceous fly ash and limestone powder. *Cem. Concr Compos.* **55**, 374–382. https://doi.org/10.1016/j.cemconcomp.2014.10.001 (2015).
12. Zunino, F. & Scrivener, K. The reaction between metakaolin and limestone and its effect in porosity refinement and mechanical properties. *Cem. Concr Res.* **140**, 106307. https://doi.org/10.1016/j.cemconres.2020.106307 (2021).
13. Avet, F. & Scrivener, K. Investigation of the calcined kaolinite content on the hydration of Limestone Calcined Clay Cement (LC3). *Cem. Concr Res.* **107**, 124–135. https://doi.org/10.1016/j.cemconres.2018.02.016 (2018).
14. EN BS. 197-5; Cement—Part 5: Portland-Composite Cement CEM II/CM and Composite Cement CEM VI. British Standards Institution: Loughborough, UK (2021).
15. Scrivener, K. et al. Impacting factors and properties of limestone calcined clay cements (LC ^{3}). *Green. Mater.* **7**, 3–14. https://doi.org/10.1680/jgrma.18.00029 (2019).
16. Antoni, M., Rossen, J., Martirena, F. & Scrivener, K. Cement substitution by a combination of metakaolin and limestone. *Cem. Concr Res.* **42**, 1579–1589. https://doi.org/10.1016/j.cemconres.2012.09.006 (2012).
17. Dhandapani, Y., Sakthivel, T., Santhanam, M., Gettu, R. & Pillai, R. G. Mechanical properties and durability performance of concretes with Limestone Calcined Clay Cement (LC3). *Cem. Concr Res.* **107**, 136–151. https://doi.org/10.1016/j.cemconres.2018.02.005 (2018).
18. Sun, J., Zunino, F. & Scrivener, K. Hydration and phase assemblage of limestone calcined clay cements (LC3) with clinker content below 50%. *Cem. Concr Res.* **177**, 107417. https://doi.org/10.1016/j.cemconres.2023.107417 (2024).

19. Li, Y., Li, Y., Ma, H. & Li, J. The hydration, microstructure, and mechanical properties of vaterite calcined clay cement (VC3). *Cem. Concr Res.* **175**, 107374. https://doi.org/10.1016/j.cemconres.2023.107374 (2024).
20. Hargis, C. W., Telesca, A. & Monteiro, P. J. M. Calcium sulfoaluminate (Ye'elimite) hydration in the presence of gypsum, calcite, and vaterite. *Cem. Concr Res.* **65**, 15–20. https://doi.org/10.1016/j.cemconres.2014.07.004 (2014).
21. Hargis, C. W. et al. Calcium Carbonate Cement: A Carbon Capture, Utilization, and Storage (CCUS) Technique. *Materials* **14**, 2709. https://doi.org/10.3390/ma14112709 (2021).
22. Zappa, W. Pilot-scale experimental work on the production of precipitated calcium carbonate (PCC) from steel slag for CO2 fixation; Aalto University: Finland, ; (Master dissertation) (2014). https://aaltodoc.aalto.fi/handle/123456789/14223
23. Mattila, H-P., Hudd, H. & Zevenhoven, R. Cradle-to-gate life cycle assessment of precipitated calcium carbonate production from steel converter slag. *J. Clean. Prod.* **84**, 611–618. https://doi.org/10.1016/j.jclepro.2014.05.064 (2014).
24. Mehdizadeh, H., Mo, K. H. & Ling, T-C. CO2-fixing and recovery of high-purity vaterite CaCO3 from recycled concrete fines. *Resour. Conserv. Recycl.* **188**, 106695. https://doi.org/10.1016/j.resconrec.2022.106695 (2023).
25. Song, Q., Guo, M-Z. & Ling, T-C. Synthesis of High-Purity and Stable Vaterite Via Leaching–Carbonation of Basic Oxygen Furnace Slag. *ACS Sustain. Chem. Eng.* **12**, 4081–4091. https://doi.org/10.1021/acssuschemeng.3c07375 (2024).
26. Guo, B. et al. Synthesis of vaterite CaCO 3 micro-spheres by carbide slag and a novel CO 2 -storage material. *J. CO2 Utilization*. **18**, 23–29. https://doi.org/10.1016/j.jcou.2017.01.004 (2017).
27. Lu, B., Zhou, Y., Jiang, L., Liu, Z. & Hou, G. High-purity vaterite CaCO3 recovery through wet carbonation of magnesium slag and leaching residue utilization in cement. *Cem. Concr Compos.* **145**, 105353. https://doi.org/10.1016/j.cemconcomp.2023.105353 (2024).
28. Chen, P. et al. Producing vaterite by CO2 sequestration in the waste solution of chemical treatment of recycled concrete aggregates. *J. Clean. Prod.* **149**, 735–742. https://doi.org/10.1016/j.jclepro.2017.02.148 (2017).
29. Avet, F., Snellings, R., Alujas Diaz, A., Ben Haha, M. & Scrivener, K. Development of a new rapid, relevant and reliable (R3) test method to evaluate the pozzolanic reactivity of calcined kaolinitic clays. *Cem. Concr Res.* **85**, 1–11. https://doi.org/10.1016/j.cemconres.2016.02.015 (2016).
30. Maraghechi, H., Avet, F., Wong, H., Kamyab, H. & Scrivener, K. Performance of Limestone Calcined Clay Cement (LC3) with various kaolinite contents with respect to chloride transport. *Mater. Struct.* **51**, 125. https://doi.org/10.1617/s11527-018-1255-3 (2018).
31. Favier, A. & Scrivener, K. Alkali silica reaction and sulfate attack: Expansion of limestone calcined clay cement. Calcined Clays for Sustainable Concrete: Proceedings of the 2nd International Conference on Calcined Clays for Sustainable Concrete, Springer; pp. 165–9. (2018).
32. Rodriguez, C. & Tobon, J. I. Influence of calcined clay/limestone, sulfate and clinker proportions on cement performance. *Constr. Build. Mater.* **251**, 119050. https://doi.org/10.1016/j.conbuildmat.2020.119050 (2020).
33. Cardinaud, G. et al. Calcined clay – Limestone cements: Hydration processes with high and low-grade kaolinite clays. *Constr. Build. Mater.* **277**, 122271. https://doi.org/10.1016/j.conbuildmat.2021.122271 (2021).
34. Krishnan, S. & Bishnoi, S. A numerical approach for designing composite cements with calcined clay and limestone. *Cem. Concr Res.* **138**, 106232. https://doi.org/10.1016/j.cemconres.2020.106232 (2020).
35. Ez-zaki, H. et al. A Fresh View on Limestone Calcined Clay Cement (LC3) Pastes. *Materials* **14**, 3037. https://doi.org/10.3390/ma14113037 (2021).
36. Nair, N., Mohammed Haneefa, K., Santhanam, M. & Gettu, R. A study on fresh properties of limestone calcined clay blended cementitious systems. *Constr. Build. Mater.* **254**, 119326. https://doi.org/10.1016/j.conbuildmat.2020.119326 (2020).
37. Hou, P. et al. Mechanisms dominating thixotropy in limestone calcined clay cement (LC3). *Cem. Concr Res.* **140**, 106316. https://doi.org/10.1016/j.cemconres.2020.106316 (2021).
38. Zunino, F. & Scrivener, K. Assessing the effect of alkanolamine grinding aids in limestone calcined clay cements hydration. *Constr. Build. Mater.* **266**, 121293. https://doi.org/10.1016/j.conbuildmat.2020.121293 (2021).
39. Zunino, F. & Scrivener, K. Microstructural developments of limestone calcined clay cement (LC3) pastes after long-term (3 years) hydration. *Cem. Concr Res.* **153**, 106693. https://doi.org/10.1016/j.cemconres.2021.106693 (2022).
40. Avet, F., Li, X. & Scrivener, K. Determination of the amount of reacted metakaolin in calcined clay blends. *Cem. Concr Res.* **106**, 40–48. https://doi.org/10.1016/j.cemconres.2018.01.009 (2018).
41. Huang, H., Li, X., Avet, F., Hanpongpun, W. & Scrivener, K. Strength-promoting mechanism of alkanolamines on limestone-calcined clay cement and the role of sulfate. *Cem. Concr Res.* **147**, 106527. https://doi.org/10.1016/j.cemconres.2021.106527 (2021).
42. Dhandapani, Y. & Santhanam, M. Assessment of pore structure evolution in the limestone calcined clay cementitious system and its implications for performance. *Cem. Concr Compos.* **84**, 36–47. https://doi.org/10.1016/j.cemconcomp.2017.08.012 (2017).
43. European Committee for Standardization. Methods of Testing Cement. Part 1: Determination of Strength, UNE-EN 196-1. Brussels, Belgium: (2018).
44. Baueregger, S., Perello, M. & Plank, J. Role of PVOH and kaolin on colloidal stability of liquid and powder EVA and SB latexes in cement pore solution. *Colloids Surf. Physicochem Eng. Asp.* **434**, 145–153. https://doi.org/10.1016/j.colsurfa.2013.05.047 (2013).
45. Rubio-Aguinaga, A., Fernández, J. M., Navarro-Blasco, Í. & Álvarez, J. I. Air lime renders with microencapsulated phase change materials: Assessment of microstructural and thermal properties. *Constr. Build. Mater.* **452**, 138862. https://doi.org/10.1016/j.conbuildmat.2024.138862 (2024).
46. European Committee for Standardization. Methods of Test for Mortar for Masonry. Part 3: Determination of Consistence of Fresh Mortar (by Flow Table) UNE-EN 1015-3. Brussels, Belgium: (2006).
47. European Committee for Standardization. Methods of test for mortar for masonry - Part 9: Determination of workable life and correction time of fresh mortar UNE-EN 1015-9. Brussels, Belgium: (2000).
48. ASTM International. Standard Test Method for Compressive Strength of Cylindrical Concrete Specimens, ASTM C39/C39M. West Conshohocken: (2016).
49. Pillai, R. G. et al. Service life and life cycle assessment of reinforced concrete systems with limestone calcined clay cement (LC3). *Cem. Concr Res.* **118**, 111–119. https://doi.org/10.1016/j.cemconres.2018.11.019 (2019).
50. Benhelal, E., Zahedi, G., Shamsaei, E. & Bahadori, A. Global strategies and potentials to curb CO2 emissions in cement industry. *J. Clean. Prod.* **51**, 142–161. https://doi.org/10.1016/j.jclepro.2012.10.049 (2013).
51. Shen, W. et al. Quantifying CO2 emissions from China's cement industry. *Renew. Sustain. Energy Rev.* **50**, 1004–1012. https://doi.org/10.1016/j.rser.2015.05.031 (2015).
52. Gettu, R. et al. Influence of supplementary cementitious materials on the sustainability parameters of cements and concretes in the Indian context. *Mater. Struct.* **52**, 10. https://doi.org/10.1617/s11527-019-1321-5 (2019).
53. Wang, Y., Zafar, I., Rashid, K., Ltifi, M. & Ju, M. Multicriteria analysis for quantifying sustainability of developed load bearing lightweight geopolymer. *J. Clean. Prod.* **434**, 140266. https://doi.org/10.1016/j.jclepro.2023.140266 (2024).
54. Qoku, E., Bier, T. A., Schmidt, G. & Skibsted, J. Impact of sulphate source on the hydration of ternary pastes of Portland cement, calcium aluminate cement and calcium sulphate. *Cem. Concr Compos.* **131**, 104502. https://doi.org/10.1016/j.cemconcomp.2022.104502 (2022).
55. Scrivener, K., Snellings, R. & Lothenbach, B. (eds) *A Practical Guide to Microstructural Analysis of Cementitious Materials* (CRC, 2018). https://doi.org/10.1201/b19074

56. Mori, Y., Enomae, T. & Isogai, A. Preparation of pure vaterite by simple mechanical mixing of two aqueous salt solutions. *Mater. Sci. Engineering: C.* **29**, 1409–1414. https://doi.org/10.1016/j.msec.2008.11.009 (2009).
57. Shen, Q. et al. Properties of Amorphous Calcium Carbonate and the Template Action of Vaterite Spheres. *J. Phys. Chem. B.* **110**, 2994–3000. https://doi.org/10.1021/jp055063o (2006).
58. Beuvier, T. et al. Synthesis of hollow vaterite CaCO3 microspheres in supercritical carbon dioxide medium. *J. Mater. Chem.* **21**, 9757. https://doi.org/10.1039/c1jm10770d (2011).
59. Kim, S., Jeon, J. & Kim, M-J. Vaterite production and particle size and shape control using seawater as an indirect carbonation solvent. *J. Environ. Chem. Eng.* **10**, 107296. https://doi.org/10.1016/j.jece.2022.107296 (2022).
60. Maslen, E. N., Streltsov, V. A. & Streltsova, N. R. X-ray study of the electron density in calcite, $CaCo_3$. *Acta Crystallogr. B.* **49**, 636–641. https://doi.org/10.1107/S0108768193002575 (1993).
61. Kamhi, S. R. On the structure of vaterite $CaCO_3$. *Acta Crystallogr.* **16**, 770–772. https://doi.org/10.1107/S0365110X63002000 (1963).
62. Muzenda, T. R., Hou, P., Kawashima, S., Sui, T. & Cheng, X. The role of limestone and calcined clay on the rheological properties of LC3. *Cem. Concr Compos.* **107**, 103516. https://doi.org/10.1016/j.cemconcomp.2020.103516 (2020).
63. Mehdizadeh, H. & Ling, T-C. Hydration and strength of cement paste containing metastable vaterite derived from recycled concrete fines and CO2. *Cem. Concr Res.* **194**, 107891. https://doi.org/10.1016/j.cemconres.2025.107891 (2025).
64. Schulze, S. E. & Rickert, J. Suitability of natural calcined clays as supplementary cementitious material. *Cem. Concr Compos.* **95**, 92–97. https://doi.org/10.1016/j.cemconcomp.2018.07.006 (2019).
65. Peng, L. et al. Mechanism underlying early hydration kinetics of carbonated recycled concrete fines-ordinary portland cement (CRCF-OPC) paste. *Cem. Concr Compos.* **144**, 105275. https://doi.org/10.1016/j.cemconcomp.2023.105275 (2023).
66. Humagain, S., Shrestha, G., Madhavan, M. K. & Sarker, P. K. Hydration, Soundness, and Strength of Low Carbon LC3 Mortar Using Waste Brick Powder as a Source of Calcined Clay. *Materials* **18**, 3697. https://doi.org/10.3390/ma18153697 (2025).
67. Abdulqader, M. et al. Physicochemical properties of limestone calcined clay cement (LC3) concrete made using Saudi clays. *J. Mater. Res. Technol.* **25**, 2769–2783. https://doi.org/10.1016/j.jmrt.2023.06.114 (2023).
68. Kafodya, I. et al. Mechanical Performance and Physico-Chemical Properties of Limestone Calcined Clay Cement (LC3) in Malawi. *Buildings* **13**, 740. https://doi.org/10.3390/buildings13030740 (2023).
69. Kim, S., Jeon, J. & Kim, M-J. Vaterite production and particle size and shape control using seawater as an indirect carbonation solvent. *J. Environ. Chem. Eng.* **10**, 107296. https://doi.org/10.1016/j.jece.2022.107296 (2022).
70. Milner, M. P., Chen, H., Yang, J. M. & Compton, R. G. Dissolution Kinetics of Solid Particles and the Role of Aggregation: Vaterite Dissolution. *J. Phys. Chem. C.* **129**, 6316–6321. https://doi.org/10.1021/acs.jpcc.5c01202 (2025).
71. Matschei, T., Lothenbach, B. & Glasser, F. P. The role of calcium carbonate in cement hydration. *Cem. Concr Res.* **37**, 551–558. https://doi.org/10.1016/j.cemconres.2006.10.013 (2007).
72. Lawrence, P., Cyr, M. & Ringot, E. Mineral admixtures in mortars effect of type, amount and fineness of fine constituents on compressive strength. *Cem. Concr Res.* **35**, 1092–1105. https://doi.org/10.1016/j.cemconres.2004.07.004 (2005).
73. Zhou, Z., Chen, B. & Ahmad, M. R. Ultra-low clinker cementitious binders with enhanced early strength via Ca(OH)2 and calcium formate activation. *Constr. Build. Mater.* **493**, 143276. https://doi.org/10.1016/j.conbuildmat.2025.143276 (2025).
74. Zunino, F. et al. Hydration and mixture design of calcined clay blended cements: review by the RILEM TC 282-CCL. *Mater. Struct.* **55**, 234. https://doi.org/10.1617/s11527-022-02060-1 (2022).
75. Zajac, M., Rossberg, A., Le Saout, G. & Lothenbach, B. Influence of limestone and anhydrite on the hydration of Portland cements. *Cem. Concr Compos.* **46**, 99–108. https://doi.org/10.1016/j.cemconcomp.2013.11.007 (2014).

Acknowledgements

The authors express their gratitude for the technical support provided by Cristina Luzuriaga and Marta Yárnoz Martín.Funding: This work was co-funded by the European Union's Horizon Europe research and innovation programme, [Grant Agreement No 101123293] (SINCERE- The Second Life of Modern Period Architecture: Resilient and Adaptive Renovation towards Net-Zero Carbon Heritage Buildings; and by Gobierno de Navarra [Grant Number PC24-007-004 ECO-HEAT].

Author contributions

Conceptualization, J.I.Á., Í.N.-B., J.M.F., L.K. and M.H.N.; data curation, M.H.N. and Í.N.-B.; formal analysis, M.H.N.; funding acquisition, J.I.Á. and Í.N.-B; investigation, M.H.N., L.K.; methodology, M.H.N., Í.N.-B.; project administration, J.I.Á. and Í.N.-B.; resources, J.M.F., Í.N.-B., and J.I.Á.; supervision, J.I.Á. and Í.N.-B.; validation, M.H.N.; visualization, M.H.N. and J.I.Á.; writing—original draft preparation, M.H.N.; writing—review and editing, L.K., J.M.F. and J.I.Á. All authors have read and agreed to the published version of the manuscript.

Funding

This work was co-funded by the European Union's Horizon Europe research and innovation programme, [Grant Agreement No 101123293] (SINCERE- The Second Life of Modern Period Architecture: Resilient and Adaptive Renovation towards Net-Zero Carbon Heritage Buildings; and by Gobierno de Navarra [Grant Number PC24-007-004 ECO-HEAT].

Declarations

Competing interests

The authors declare no competing interests.

Additional information

Supplementary Information The online version contains supplementary material available at https://doi.org/10.1038/s41598-026-51241-3.

Correspondence and requests for materials should be addressed to J.I.Á.

Reprints and permissions information is available at www.nature.com/reprints.

Publisher's Note Springer Nature remains neutral with regard to jurisdictional claims in published maps and institutional affiliations.

Open Access This article is licensed under a Creative Commons Attribution-NonCommercial-NoDerivatives 4.0 International License, which permits any non-commercial use, sharing, distribution and reproduction in any medium or format, as long as you give appropriate credit to the original author(s) and the source, provide a link to the Creative Commons licence, and indicate if you modified the licensed material. You do not have permission under this licence to share adapted material derived from this article or parts of it. The images or other third party material in this article are included in the article's Creative Commons licence, unless indicated otherwise in a credit line to the material. If material is not included in the article's Creative Commons licence and your intended use is not permitted by statutory regulation or exceeds the permitted use, you will need to obtain permission directly from the copyright holder. To view a copy of this licence, visit http://creativecommons.org/licenses/by-nc-nd/4.0/.

© The Author(s) 2026